1
Modeling Catalytic Reactions on Surfaces with Density Functional Theory

*John A. Keith, Josef Anton, Payam Kaghazchi, and Timo Jacob*

1.1
Introduction

Predicting the reactivity of catalytic systems is a nontrivial process that usually requires knowledge about its geometric and electronic structure, properties determined by quantum mechanics (QM). Solving the Schrödinger equation[1] is a nontrivial task even for small systems, and it becomes especially arduous when the system involves multiple phases as is the case in a surface reaction. Theoretical calculations nevertheless provide useful and important perspectives on chemical reactions that are not accessible through experimental observations alone. Figure 1.1 schematically shows the hierarchy of multiscale modeling, starting from the subatomic regime, over the electronic and atomistic regimes, to the meso- and finally the macroscale. Different theoretical methods have been established to address questions related to each regime (or timescale and length scale); however, realistic processes usually involve effects from all scales. In this chapter, we will focus on the electronic and atomistic regimes, which not only provide the basis for climbing up the hierarchy of multiscale modeling but also provide important mechanistic information on catalytic reactions.

Quantum chemistry is the application of QM to better understand chemical systems. In its purest form, QM calculations solve the Schrödinger equation, which provides the energy of a given configuration of nuclei and their electrons. There are two general approaches to do this. One way is to solve the energy given by the Schrödinger equation approximately using a nonclassical wavefunction. Another popular approach, density functional theory (DFT), uses the electronic density to evaluate the energy of a system via an approximate functional. Both approaches have their merits and provide a nonthermodynamical representation of the energy of a system of electrons.

This chapter gives an introductory overview of the essential concepts behind theoretical calculations of surface reactions, which we then apply to better understand one of the key features in energy conversion and fuel cell technology:

---

[1] For the relativistic case, one has to consider the Dirac equation.
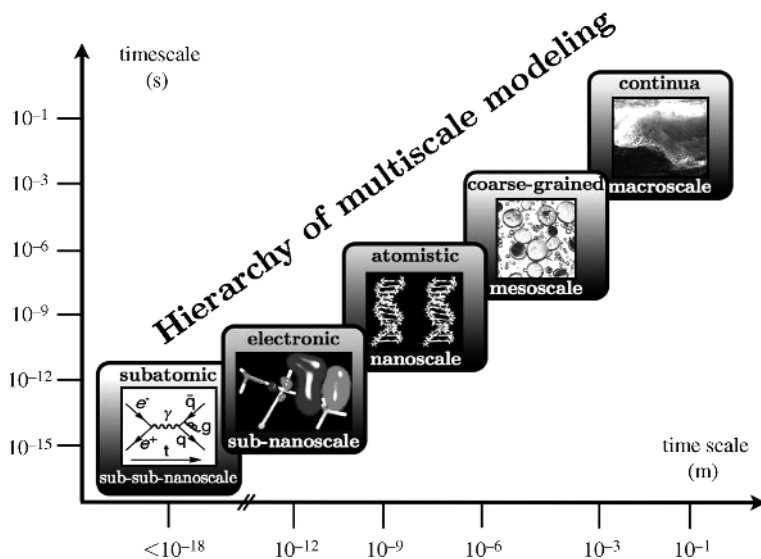
Figure 1.1 Hierarchy of multiscale modeling of different time and length regimes.

the electrocatalytic oxygen reduction reaction (ORR). After describing the multibody problem in quantum mechanics, we will discuss the fundamentals behind wave function- and density-based methods used to solve this problem. We will then focus on density functional theory and its advantages and disadvantages in applications to catalysis. Section 1.2, the first part of this chapter, ends with brief technical details one has to grapple with when modeling surface reactions. This includes thermodynamic approximations and other considerations that extend calculated values from theoretical studies to be more comparable to experiment. Section 1.3, the second part of this chapter, shows an example how quantum mechanical DFT calculations can resolve mechanistic details of a rather complex surface reaction.

1.2
Theoretical Background

1.2.1
The Many-Body Problem

Many material properties of interest to physicists and chemists can be obtained by solving the many-body Schrödinger equation. In stationary, nonrelativistic terms it can be written as

$$\hat{H}\Psi(\mathbf{r}_i\sigma_i, \mathbf{R}_\nu) = E\Psi(\mathbf{r}_i\sigma_i, \mathbf{R}_\nu), \tag{1.1}$$

where $\hat{H}$ is the Hamilton operator, $\Psi(\mathbf{r}_i\sigma_i, \mathbf{R}_\nu)$ is the many-body wave function, E is the total energy of the system, σ_i is the spin coordinate of electron i, and finally $\mathbf{r}_i$

and $\mathbf{R}_\nu$ are the spatial coordinates of electron i and nucleus ν, respectively. The Hamiltonian for a system consisting of a set of nuclei and electrons can be written as[2]

$$\hat{H} = \sum_{\nu=1}^{N} \hat{T}_\nu + \underbrace{\sum_{i=1}^{M} \hat{t}_i - \sum_{i=1}^{M}\sum_{\nu=1}^{N} \frac{Z_\nu}{|\mathbf{r}_i - \mathbf{R}_\nu|} + \frac{1}{2}\sum_{\substack{i,j=1 \\ i\neq j}}^{M} \frac{1}{|\mathbf{r}_i - \mathbf{r}_j|}}_{\hat{H}_e} + \frac{1}{2}\sum_{\substack{\nu,\mu=1 \\ \nu\neq\mu}}^{N} \frac{Z_\nu Z_\mu}{|\mathbf{R}_\nu - \mathbf{R}_\mu|},$$

(1.2)

where $\hat{T}_\nu$ and $\hat{t}_i$ are the respective kinetic energy operators for nuclei and electrons, and Z_ν is the charge on a nucleus. The two species (electrons and nuclei) interact with each other and themselves. It is difficult to solve such a coupled system since the motion of any particle is influenced by all other particles. Except for simple systems such as a hydrogen atom, solving Eq. (1.1) with the corresponding Hamiltonian, Eq. (1.2), is nontrivial for most materials that consist of several electrons and nuclei. Therefore, simulations of realistic systems require different applications of approximations.

1.2.2
Born–Oppenheimer Approximation

The Born–Oppenheimer (BO) approximation (introduced by Max Born and J. Robert Oppenheimer in 1927 [1]) treats the electronic and nuclear degrees of freedom as decoupled from each other. Nuclei are much more massive than electrons, so electrons are assumed to instantaneously follow the motion of the nuclei. Consequently, on the timescale of the motion of the electrons, the nuclei appear almost stationary. The total wave function of Eq. (1.1) can then be written as[3]

$$\Psi(\mathbf{r}_i\sigma_i, \mathbf{R}_\nu) = \psi_e(\mathbf{r}_i\sigma_i, \{\mathbf{R}_\nu\})\psi_n(\mathbf{R}_\nu)$$

(1.3)

where $\psi_e(\mathbf{r}_i\sigma_i, \{\mathbf{R}_\nu\})$ and $\psi_n(\mathbf{R}_\nu)$ are the electronic and nuclei wave functions, and $\{\mathbf{R}_\nu\}$ denotes that nuclear spatial coordinates are parameters and not variables. We then can divide the electronic and nuclear parts into

$$\hat{H}_e \psi_e(\mathbf{r}_i\sigma_i, \{\mathbf{R}_\nu\}) = \left(-\sum_{i=1}^{M} \frac{1}{2}\nabla_i^2 + \frac{1}{2}\sum_{\substack{i,j=1 \\ i\neq j}}^{M} \frac{1}{|\mathbf{r}_i - \mathbf{r}_j|} - \sum_{i=1}^{M}\sum_{\nu=1}^{N} \frac{Z_\nu}{|\mathbf{r}_i - \mathbf{R}_\nu|} \right) \psi_e(\mathbf{r}_i\sigma_i, \{\mathbf{R}_\nu\})$$

$$= E_e(\mathbf{R}_\nu)\psi_e(\mathbf{r}_i\sigma_i, \{\mathbf{R}_\nu\})$$

(1.4)

---

2) Throughout this chapter, atomic units are assumed.

3) This is an expansion of $\Psi(\mathbf{r}_i\sigma_i, \mathbf{R}_\nu)$ in a series of eigenfunctions of the electronic Hamilton operator $\hat{H}_e$. Since in chemistry electronic excitations usually do not play a substantial role, we restrict our discussion to the eigenfunctions with the lowest energy of the electronic system (ground state) $\psi_e(\mathbf{r}_i\sigma_i, \{\mathbf{R}_\nu\})$.

and

$$\left(-\sum_{\nu=1}^{N} \frac{1}{2m_\nu} \nabla_\nu^2 + \frac{1}{2} \sum_{\substack{\nu,\mu=1 \\ \nu \neq \mu}}^{N} \frac{Z_\nu Z_\mu}{|\mathbf{R}_\nu - \mathbf{R}_\mu|} + E_e(\mathbf{R}_\nu) \right) \psi_n(\mathbf{R}_\nu) = E\psi_n(\mathbf{R}_\nu). \qquad (1.5)$$

In Eq. (1.4), $\hat{H}_e$ and ψ_e depend only on the positions of the nuclei. In the case of negligible nonadiabatic effects, this approximation introduces a very small error into the energies, and this inaccuracy becomes even smaller for heavier elements [2]. Applying this approximation, we can restrict ourselves to the electronic part[4] (Eq. (1.4)), which can be solved exactly for one-electron systems only. Thus, we need further approximations for systems with many electrons. Many techniques solve the Schrödinger equation approximately from first principles (*ab initio*). Two common types of *ab initio* methods are the wave function-based and the density-based approaches [3]. Both have been applied extensively in material science and catalysis.

1.2.3
Wave Function-Based Methods

The Born–Oppenheimer approximation reduces the many-body problem to the electronic part only (with the positions of the nuclei as parameters), but the electronic wave function is still a function of the spatial coordinates of the electrons and their spin variables. We now describe the Hartree–Fock (HF) approximation, which can be viewed as the basis for all practical *ab initio* developments. This approach does not include any correlation effects, and we will later describe different approaches to account for these.

1.2.3.1 Hartree–Fock Approximation
In 1927, Hartree [4] considered the electron motions as independent (uncorrelated). Each electron could then be treated as moving in an averaged field originating from all other electrons.[5] Three years later, Fock [5] followed Hartree's idea to express the overall electronic wave function as simple product of single-particle wave functions, but he introduced the fermionic character of the electrons by using an antisymmetric sum product of single-particle wave functions. The most simple *ansatz* for such a representation is given by a single Slater determinant [6]:

$$\psi_e = \frac{1}{\sqrt{M!}} \begin{vmatrix} \varphi_1(\mathbf{r}_1\sigma_1) & \varphi_1(\mathbf{r}_2\sigma_2) & \dots & \varphi_1(\mathbf{r}_M\sigma_M) \\ \varphi_2(\mathbf{r}_1\sigma_1) & \varphi_2(\mathbf{r}_2\sigma_2) & \dots & \varphi_2(\mathbf{r}_M\sigma_M) \\ \vdots & \vdots & & \vdots \\ \varphi_M(\mathbf{r}_1\sigma_1) & \varphi_M(\mathbf{r}_2\sigma_2) & \dots & \varphi_M(\mathbf{r}_M\sigma_M) \end{vmatrix}, \qquad (1.6)$$

where $\varphi_i(\mathbf{r}_j\sigma_j)$ describes electron i at the position of electron j. According to Ritz [7], the lowest-energy system state corresponds to the ground state, which is obtainable

---

4) Although Eq. (1.4) is the main electronic contribution, in practice we usually also consider the second term of Eq. (1.5).

5) This is usually called the model of independent electrons or the effective one-particle model.

by variation under the constraint of an orthonormal[6] set of single-particle wave functions $\varphi_i(\mathbf{r}_j \sigma_j)$:

$$\delta \left\{ E_e - \sum_{i,j=1}^{M} \varepsilon_{ij} \langle \varphi_i | \varphi_j \rangle \right\} = 0. \tag{1.7}$$

This finally leads to the well-known Hartree–Fock equations:

$$\hat{F}(\mathbf{r}_i) | \varphi_i \rangle = \sum_{j=1}^{M} \varepsilon_{ij} | \varphi_j \rangle, \quad i = 1, 2, \ldots, M. \tag{1.8}$$

Here, $\hat{F}$ is the Fock operator, which can be written as[7]

$$\hat{F}(\mathbf{r}_i) = \hat{t}_i - \sum_{\nu=1}^{N} \frac{Z_\nu}{|\mathbf{r}_i - \mathbf{R}_\nu|} + \sum_{j=1}^{M} \int \varphi_j^*(\mathbf{r}') \frac{1}{|\mathbf{r}_i - \mathbf{r}'|} \varphi_j(\mathbf{r}') \, d\mathbf{r}' + V_x(\mathbf{r}_i). \tag{1.9}$$

The last term originates from the Pauli principle and describes the nonlocal exchange, for which there is no classical analogue:

$$V_x(\mathbf{r}_i) = - \sum_{j=1}^{M} \int \frac{1}{|\mathbf{r}_i - \mathbf{r}'|} \frac{\varphi_j^*(\mathbf{r}') \varphi_j(\mathbf{r}_i) \varphi_i^*(\mathbf{r}_i) \varphi_i(\mathbf{r}')}{\varphi_i^*(\mathbf{r}_i) \varphi_i(\mathbf{r}_i)} d\mathbf{r}'. \tag{1.10}$$

Due to the aforementioned nonlocal character of the exchange, practical calculation of this term is extremely demanding. Dirac [8] and Bloch [9] independently showed that the exchange integral for a free electron gas can be expressed as function of the electronic density. In order to generalize this idea, Slater [10, 11] added a scaling factor X_α to the expression for the free electron gas

$$V_x(\mathbf{r}_i) = -3 X_\alpha \left(\frac{3}{8\pi} \varrho(\mathbf{r}_i) \right)^{1/3}. \tag{1.11}$$

For the free electron gas, the scaling factor is 2/3. However, a value of $X_\alpha = 0.7$ led to an improved accuracy for atoms [12, 13].

Insertion of the Slater approximation into the exchange term of the HF equations finally leads to the so-called Hartree–Fock–Slater equation (HFS).

1.2.3.2 Post Hartree–Fock Methods

A critical shortcoming of HF theory is its lack of *electronic correlation*, that is, the treatment of systems of electrons interacting with each other. This correlation is often separated into two parts. *Dynamical* correlation relates to responsiveness of electrons interacting with each other, while *nondynamical* electronic correlation relates to how a real system's energy is due to contributions from several accessible electronic states. HF theory treats neither and is not accurate enough to make reliable chemical

---

6) In the variation, the constraints are usually included as Lagrange multipliers ε_{ij}.

7) Spin variables have not been expressed explicitly.

determinations, but additional corrections have been developed in order to account for these shortcomings such as full CI (configurational interaction), Møller–Plesset perturbation theory (MPn), complete active space (CAS), or coupled cluster (CC) methods (see Refs. [14–16] for more details). The majority of these methods are under the umbrella of fully first-principles methods, that is, *ab initio* wave function methods that incorporate no empirical data into their calculation. For problems in catalysis, most of these methods are too expensive in practice; however, the MP2 method is occasionally useful in calculating dispersion forces and van der Waals interactions.

General perturbation theory presumes that the magnitude of a perturbation in a calculation is small compared to the unperturbed value of the calculation itself. This is valid for the electron correlation energy, which is small compared to the HF energy. According to perturbation theory in quantum mechanics, the total Hamiltonian is divided into the unperturbed reference Hamiltonian ($\hat{H}_0$) plus the Hamiltonian corresponding to its correction ($\hat{H}'$) times a scaling factor λ, which determines the strength of the perturbation:

$$\hat{H} = \hat{H}_0 + \lambda \hat{H}'. \tag{1.12}$$

Based on this separation, perturbation theory yields the different terms of the Taylor expansion of the electronic energy. Consequently, the first two orders of correction to the energy of an electronic state n become

$$E_{e,n}^{(1)} = \left\langle \psi_{e,n}^{(0)} | \hat{H}' | \psi_{e,n}^{(0)} \right\rangle$$

$$E_{e,n}^{(2)} = \sum_{j \neq n} \frac{\left| \left\langle \psi_{e,n}^{(0)} | \hat{H}' | \psi_{e,j}^{(0)} \right\rangle \right|^2}{E_{e,n}^{(0)} - E_{e,j}^{(0)}} \tag{1.13}$$

In Møller–Plesset perturbation theory, $\hat{H}_0$ is taken as the sum of one-electron Fock operators. The sum of $E_{e,n}^{(0)} + E_{e,n}^{(1)}$ is the electronic HF energy,[8] and additional $E_{e,n}^{(i>1)}$ corrects the HF energy for electronic correlation. Calculations including the first additional correction $E_{e,n}^{(2)}$ are called MP2 methods, while MP3, MP4, and so on also treat higher perturbation orders.

Although Møller–Plesset perturbation theory in principle allows for a full inclusion of electronic correlations, evaluating even the first correction terms becomes quite expensive as the number of electrons in the system increases. Even nowadays, MP2 is often considered too expensive for simulating surface reactions.

1.2.4
Density-Based Methods

Instead of employing many-body wave functions, density-based methods use the electron density as the basic variable to evaluate the total energy and other properties. A well-known density-based approach is the density functional theory, which was introduced by Hohenberg and Kohn in 1964 [17] and further developed by Kohn and

---

8) In HF approximation, $E_{e,n}^{(1)} = 0$.

Sham in 1965 [18]. This method dates back to the works of Thomas and Fermi (TF). Before describing the DFT approach itself, we briefly review the TF model. Although this section focuses on the electronic part of the many-body problem, for simplicity, the index e is not given explicitly.

1.2.4.1 The Thomas–Fermi Model

The electronic part of the many-body wave function containing M electrons, $\psi(\mathbf{r}_1\sigma_1, \ldots, \mathbf{r}_M\sigma_M)$, is not easy to calculate since it depends on $4M$ coordinates ($3M$ coordinates if spin is not considered). Thomas and Fermi proposed a simpler approach, the TF model, using the electron density of the system $\varrho(\mathbf{r})$ as the basic variable [19, 20]. A key advantage of this approach is that the electron density of M electrons in a volume element $d\mathbf{r}$ depends only on three independent coordinates:

$$\varrho(\mathbf{r}) = \sum_{i=1}^{M} \int \psi(\mathbf{r}_1\sigma_1, \ldots, \mathbf{r}_M\sigma_M)^* \delta(\mathbf{r}_i - \mathbf{r})\psi(\mathbf{r}_1\sigma_1, \ldots, \mathbf{r}_M\sigma_M) d(\mathbf{r}_1\sigma_1) \ldots d(\mathbf{r}_M\sigma_M).$$

$$(1.14)$$

Here, the ground-state total energy and other properties can be expressed as functionals of the electron density. By assuming that the kinetic energy density is locally equal to that of a homogeneous electron gas, Thomas and Fermi formulated the total energy functional $E^{\mathrm{TF}}[\varrho(\mathbf{r})]$ as

$$E^{\mathrm{TF}}[\varrho(\mathbf{r})] = \frac{3(3\pi^2)^{2/3}}{10} \int \varrho(\mathbf{r})^{5/3} d\mathbf{r} - \sum_{\nu=1}^{N} \frac{Z_\nu \varrho(\mathbf{r})}{|\mathbf{r} - \mathbf{R}_\nu|} d\mathbf{r} + \frac{1}{2} \int\int \frac{\varrho(\mathbf{r})\varrho(\mathbf{r}')}{|\mathbf{r} - \mathbf{r}'|} d\mathbf{r}d\mathbf{r}'.$$

$$(1.15)$$

The first term denotes the kinetic energy of noninteracting electrons, and the second and third terms are the classical electrostatic electron–nucleus attraction and electron–electron repulsion, respectively. Later on, Dirac included the exchange energy, which has no classical analogue, as an additional term to the TF model [8]:

$$E_{\mathrm{x}}^{\mathrm{Dirac}} = -\frac{3}{4}\left(\frac{3}{\pi}\right)^{1/3} \int \varrho(\mathbf{r})^{4/3} d\mathbf{r}.$$

$$(1.16)$$

TF calculated energies are usually too high. The Thomas–Fermi–Dirac (TFD) model accounts for this by adding an appropriate exchange term that gives a negative energy contribution. Despite this correction, calculated total energies are still not accurate for chemical predictions since the kinetic energy is poorly described. Although the TF model was not very successful in quantum chemistry or solid-state physics, it is the starting point for DFT in the sense of using the electron density for solving multielectron systems.

1.2.4.2 The Hohenberg–Kohn Theorems

The theoretical basis of DFT are two fundamental theorems, which were formulated and mathematically proven by Hohenberg and Kohn [17] for nondegenerate ground states. According to the first theorem, the electron density uniquely determines the

external potential (the potential of the ions or nuclei) to within a constant. Therefore, the total electronic energy of a system E can be expressed as a functional of the electron density ϱ,

$$E[\varrho] = T[\varrho] + \int \varrho(\mathbf{r}) V_{\text{ext}}(\mathbf{r}) d\mathbf{r} + E_{\text{ee}}[\varrho], \tag{1.17}$$

where $T[\varrho]$ is the kinetic energy functional and $E_{\text{ee}}[\varrho]$ is the electron–electron interaction energy and also a functional. By defining the Hohenberg–Kohn functional

$$F_{\text{HK}}[\varrho] = T[\varrho] + E_{\text{ee}}[\varrho], \tag{1.18}$$

we obtain

$$E[\varrho] = \int \varrho(\mathbf{r}) V_{\text{ext}}(\mathbf{r}) d\mathbf{r} + F_{\text{HK}}[\varrho]. \tag{1.19}$$

The exact solution to the Schrödinger equation could be obtained with an explicit expression for the universal functional $F_{\text{HK}}[\varrho]$. Unfortunately, this expression is still unknown, but we will later show different approximations for this term. The remaining electron–electron interaction $E_{\text{ee}}[\varrho]$ can be written as

$$E_{\text{ee}}[\varrho] = J[\varrho] + E^{\text{noncl}}[\varrho], \tag{1.20}$$

where the first term is simply the classical Coulomb repulsion and the second term is the nonclassical part that contains self-interaction correction, exchange, and Coulomb correlation energy.

The second Hohenberg–Kohn theorem provides the energy variational principle for the exact functional. The ground-state density $\varrho_0(\mathbf{r})$ is the density that minimizes $E[\varrho]$

$$E_0 = E[\varrho_0(\mathbf{r})] \leq E[\varrho(\mathbf{r})] \tag{1.21}$$

when

$$\varrho(\mathbf{r}) \geq 0 \quad \text{and} \quad \int \varrho(\mathbf{r}) d\mathbf{r} - M = 0. \tag{1.22}$$

Energy minimization of the energy functional fulfills the Euler–Lagrange equation under the constraint of a constant number of electrons M (Eq. (1.22)), which can be written as

$$\mu = \frac{\delta E[\varrho(\mathbf{r})]}{\delta \varrho(\mathbf{r})} = V_{\text{ext}}(\mathbf{r}) + \frac{\delta F_{\text{HK}}[\varrho(\mathbf{r})]}{\delta \varrho(\mathbf{r})}, \tag{1.23}$$

where the Lagrange multiplier μ is the chemical potential of the electrons. In principle, this formulation provides all ground-state properties, but the Hohenberg–Kohn theorems do not tell us how to find the universal functional $F_{\text{HK}}[\varrho]$. Later on, Kohn and Sham [18] found rather accurate approximations for $F_{\text{HK}}[\varrho]$, and others still continue this development.

1.2.4.3 The Kohn–Sham Equations

Kohn and Sham decomposed the exact kinetic energy functional $T[\varrho]$ into two parts to approximate the universal functional $F_{HK}[\varrho]$ in terms of Eq. (1.18). The first term is the kinetic energy of a system of noninteracting electrons T_s given by

$$T_s = -\frac{1}{2} \sum_{i=1}^{N} < \phi_i | \nabla^2 | \phi_i >, \qquad (1.24)$$

where ϕ_i are the so-called Kohn–Sham orbitals. The second term contains all remaining (and neglected) interactions in the noninteracting system $(T - T_s)$.

The second contribution is a small correction and it is included along with the nonclassical part of the electron–electron interaction E^{noncl} into a term defined as exchange–correlation (xc) energy:

$$E_{xc}[\varrho] = (T[\varrho] - T_s[\varrho]) + (E_{ee}[\varrho] - J[\varrho]). \qquad (1.25)$$

The energy functional Eq. (1.17) is now written as[9]

$$E[\varrho] = T_s[\varrho] + \int \varrho(\mathbf{r}) V_{ext}(\mathbf{r}) d r + J[\varrho] + E_{xc}[\varrho]. \qquad (1.26)$$

Finding suitable expressions for the $E_{xc}[\varrho]$ term is the main challenge in DFT development since it consists of all contributions that are not yet known exactly. The Euler–Lagrange equation now has the form

$$\varepsilon_i \frac{\delta \varrho(\mathbf{r})}{\delta \phi_i} = \frac{\delta E[\varrho(\mathbf{r})]}{\delta \varrho(\mathbf{r})} \frac{\delta \varrho(\mathbf{r})}{\delta \phi_i} = \frac{\delta T_s[\varrho(\mathbf{r})]}{\delta \phi_i} + V_{eff}(\mathbf{r}) \frac{\delta \varrho(\mathbf{r})}{\delta \phi_i} \qquad (1.27)$$

with

$$V_{eff}(\mathbf{r}) = V_{ext}(\mathbf{r}) + \int \frac{\varrho(\mathbf{r}')}{|\mathbf{r} - \mathbf{r}'|} d\mathbf{r}' + V_{xc}(\mathbf{r}), \qquad (1.28)$$

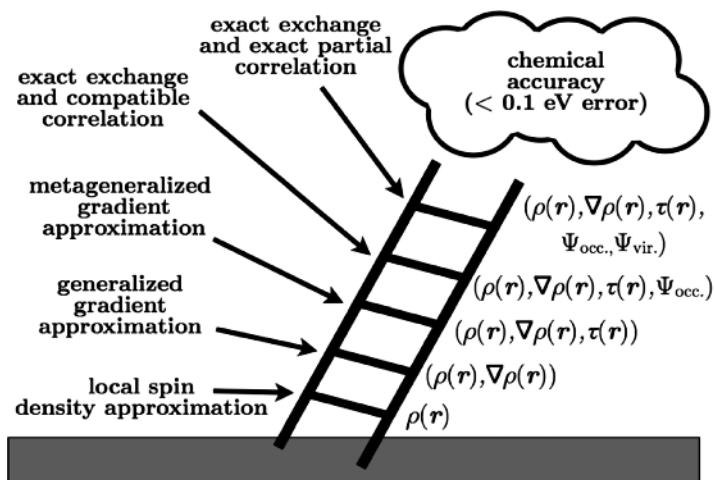where the exchange–correlation potential $V_{xc}(\mathbf{r})$ is

$$V_{xc}(\mathbf{r}) = \frac{\delta E_{xc}[\varrho(\mathbf{r})]}{\delta \varrho(\mathbf{r})}. \qquad (1.29)$$

The solution of Eq. (1.27) is obtained by solving the following set of one-particle equations

$$\left[-\frac{1}{2} \nabla^2 + V_{eff}(\mathbf{r}) \right] \phi_i = \varepsilon_i \phi_i, \qquad (1.30)$$

---

[9] In principle, the kinetic energy term T_s is a functional of the Kohn–Sham orbitals ϕ_i.

Figure 1.2 Jacob's ladder illustrating the hierarchy of exchange–correlation functionals.

where the electron density of the real system is constructed from the Kohn–Sham orbitals

$$\varrho(r) = \sum_{i=1}^{\text{occ}} |\phi_i(r)|^2. \tag{1.31}$$

Here, the summation runs over all occupied orbitals (occ). Equations (1.28), (1.30) and (1.31) are known as Kohn–Sham equations. The procedure to solve a particular problem is to start with a guessed $\varrho(\mathbf{r})$, determine V_{eff} from Eq. (1.28), and then obtain a new $\varrho(\mathbf{r})$ from Eqs. (1.30) and (1.31). This procedure is then repeated until $\varrho(\mathbf{r})$ is converged, and the total energy is obtained.[10]

1.2.4.4 Exchange–Correlation Functionals

Density-based formulations reduce the complexity of the many-body problem, but the resulting Kohn–Sham equation (1.30) still requires an xc functional. Different approximations of this term are the key distinction of all DFT implementations.

Perdew [21, 22] has illustratively formulated the hierarchy of different approximations of the xc functional as a "Jacob's ladder," rising from the earth of Hartree to the heaven of chemical accuracy (see Figure 1.2).

Starting from the earth of Hartree, the subsequent rungs of the ladder are defined as follows:

- **Local (spin) density approximation (L(S)DA):** Here the exchange–correlation energy of an inhomogeneous system is obtained by assuming that its density

---

10) This iterative process is known as the self-consistent field (SCF) approach.

can locally be treated as a uniform electron gas. The xc energy can then be written as

$$E_{xc}^{LDA}[\varrho] = \int \varrho(\mathbf{r})\varepsilon_{xc}(\varrho(\mathbf{r}))d\mathbf{r}, \tag{1.32}$$

where $\varepsilon_{xc}(\varrho(\mathbf{r}))$ is the xc energy per particle of the homogeneous electron gas, which can be split into exchange and correlation terms

$$\varepsilon_{xc}(\varrho(\mathbf{r})) = \varepsilon_x(\varrho(\mathbf{r})) + \varepsilon_c(\varrho(\mathbf{r})). \tag{1.33}$$

The exchange part is given by the Dirac expression (Eq. (1.16))

$$\varepsilon_x(\varrho(\mathbf{r})) = -\frac{3}{4}\left(\frac{3}{\pi}\right)^{1/3}\varrho(\mathbf{r})^{1/3}. \tag{1.34}$$

The correlation component ε_c has been determined by Monte Carlo (MC) calculations for a uniform electron gas considering a number of different densities [2]. Although one might expect that the LDA functional is valid only for a slowly varying density that might resemble a uniform electron gas, experience shows that this approximation is surprisingly valuable in a wide range of problems in solid-state physics and material science. LDA is noted to calculate molecular geometries and vibrational frequencies reasonably, but bond energies are strongly overestimated.

- **Generalized gradient approximation (GGA):** Inadequacies in LDA brought about a modified xc functional that, in addition to the density, contains terms for the density gradient:

$$E_{xc}^{GGA}[\varrho] = \int \varrho(\mathbf{r})\varepsilon_{xc}(\varrho(\mathbf{r}), \nabla\varrho(\mathbf{r}))d\mathbf{r}. \tag{1.35}$$

One form of GGA introduced by Perdew, Burke, and Ernzerhof (PBE) [23] is widely used in surface physics. In this approximation, the correlation energy is expressed as

$$E_c^{GGA}[\varrho] = \int \varrho\left[\varepsilon_c^{unif}(\varrho) + K(\varrho, t)\right]d\mathbf{r}, \tag{1.36}$$

with

$$K(\varrho, t) = \gamma\ln\left[1 + \frac{\beta t^2}{\gamma}\left(\frac{1 + At^2}{1 + At^2 + A^2t^4}\right)\right] \tag{1.37}$$

and

$$\gamma \simeq 0.031091; \quad \beta \simeq 0.066725; \quad A = \frac{\beta}{\gamma}\frac{1}{e^{-\varepsilon_c^{unif}/\gamma} - 1}; \quad t = \frac{|\nabla\varrho|}{2\left(\sqrt{4(3\pi^2\varrho)^{1/3}/\pi}\right)\varrho}. \tag{1.38}$$

Here, t is a dimensionless density gradient. The exchange energy in terms of an enhancement factor F_x is written as

$$E_x^{\text{GGA}}[\varrho] = \int \varrho \varepsilon_x^{\text{unif}}(\varrho) F_x(s) d\mathbf{r}, \tag{1.39}$$

where $\varepsilon_x^{\text{unif}}(\varrho)$ and $\varepsilon_c^{\text{unif}}(\varrho)$ are, respectively, the exchange and correlation energies per particle of a homogeneous electron gas at point $\mathbf{r}$ (see Eq. (1.34)) and s is another dimensionless density gradient

$$s = \frac{|\nabla \varrho|}{2(3\pi^2 \varrho)^{1/3} \varrho}. \tag{1.40}$$

Finally, the function $F_x(s)$ is

$$F_x(s) = 1 + \kappa - \frac{\kappa}{1 + \mu s^2/\kappa}, \tag{1.41}$$

where $\kappa = 0.804$ and $\mu \simeq 0.21951$.

- **Meta-generalized gradient approximation (MGGA):** The kinetic energy density, $\tau(\mathbf{r})$, is an additional Kohn–Sham contribution that can be calculated. In general, MGGA functionals have the following form:

$$E_{xc}^{\text{MGGA}}[\varrho] = \int \varrho(\mathbf{r}) \varepsilon_{xc}(\varrho(\mathbf{r}), \nabla \varrho(\mathbf{r}), \tau(\mathbf{r})) d\mathbf{r}. \tag{1.42}$$

The main advantage of including kinetic energy densities is that it mostly eliminates self-interaction errors, causing inaccuracies with LDA and GGA functionals at low-density and strong interaction limits. In intermediate regions, however, MGGA functionals usually do not provide substantial improvement to corresponding GGAs.

- **Hybrid DFT with exact exchange:** An entirely different approach to improve deficiencies in GGA functionals is to incorporate the so-called exact exchange energy (EXX) contributions. The exact exchange energy E_x^{exact} is a derivative from the Hartree–Fock approximation (see Section 2.3.1), and is obtained by solving only the exchange part of the exchange–correlation functional exactly. The result is an energy value that when scaled according to

$$E_{xc}^{\text{hybrid}} = E_{xc}^{\text{GGA}} + a\left(E_x^{\text{exact}} - E_x^{\text{GGA}}\right) \tag{1.43}$$

provides a convenient cancellation of errors, making hybrid DFT methods surprisingly accurate. Based on this idea, the highly popular hybrid DFT method B3LYP combines exact HF exchange with the Slater [24] local exchange functional. In addition, it uses the Becke gradient correction [25], the local Vosko–Wilk–Nusair exchange functional [26], and the Lee–Yang–Parr local gradient-corrected functional [27]. Inclusion of the nonlocal exchange, however, limits these methods to be applicable only for finite systems and not in a periodic representation.

1.2.5
Technical Aspects of Modeling Catalytic Reactions

1.2.5.1 Geometry Optimizations

The following discussion of atomic properties in molecular configurations is simplified by considering a Born–Oppenheimer potential energy surface (PES). The PES is a hypersurface that is defined by the electronic energy as a function of the nuclei positions R_ν, which are $3N$ dimensional.[11] We now concentrate on the electronic part of the total energy that depends on the atom positions as parameters plus the nuclei–nuclei interaction ($E_e + E_{n-n}$). A PES can be expressed in the neighborhood of any spatial position R_ν^0 as

$$E(\mathbf{R}_\nu) = E\left(\mathbf{R}_\nu^0\right) + g\left(\mathbf{R}_\nu - \mathbf{R}_\nu^0\right) + \frac{1}{2}\left(\mathbf{R}_\nu - \mathbf{R}_\nu^0\right)^{\mathrm{T}}\mathbf{H}\left(\mathbf{R}_\nu - \mathbf{R}_\nu^0\right) + \dots, \tag{1.44}$$

where g and $\mathbf{H}$ are the gradients and Hesse matrix (or Hessian), whose components are defined as

$$g_\nu = \left.\frac{\partial E}{\partial \mathbf{R}_\nu}\right|_{\mathbf{R}_\nu = \mathbf{R}_\nu^0} \quad \text{and} \quad H_{\nu\mu} = \left.\frac{\partial^2 E}{\partial \mathbf{R}_\nu \partial \mathbf{R}_\mu}\right|_{\mathbf{R}_\nu = \mathbf{R}_\nu^0}. \tag{1.45}$$

While gradient calculations are typically manageable for large-scale calculations, Hessian calculations can be enormously time consuming.

After an electronic energy is calculated, a gradient calculation can be performed analytically or numerically. With this gradient, a cycle of procedures using any of the multitude of optimization schemes can change the atomic positions of the molecule R_ν until the gradient has reached a small value (below the desired convergence threshold), thereby indicating a stationary point on the PES. This process of calculating a gradient (and then adjusting the atomic positions accordingly) from an energy is usually referred to as geometry optimization step. Common procedures for geometry optimizations include the *steepest descent*, *conjugate gradient*, *Newton–Raphson*, or *Broyden–Fletcher–Goldfarb–Shanno(BFGS)* methods (see Ref. [28] for more details), some of which require only the first derivative of the energy or even use the Hesse matrix (see Eqs. (1.44) and (1.45)). Although each method has certain benefits, all are simply algorithms to reach the desired low-energy state faster in lieu of troublesome regions of the topology of the PES.

Stationary points define stable intermediates when located at a local minimum of the PES. In practice, geometry optimizations are accelerated by force constants associated with normal modes of the species at different points of the PES, and these force constants can be obtained from the Hessian. To avoid the expense of calculating a Hessian at every geometry iteration, methods are available to construct approximate Hessians from gradient calculations. The integrity of these Hessians is not always ideal, often still requiring a full (numerical) calculation of the Hessian at the end of the geometry optimization.

---

11) Note that this is not describing an *internal* coordinate system where one omits six coordinates related to system translations and rotations to result in $3N-6$ coordinates.

1.2.5.2 Transition-State Optimizations

Geometry optimizations can also be extended to seek transition states (TS), first-order saddle points where all but one internal coordinate are at a minimum. Unfortunately, these approaches are substantially more difficult since the local topology of a PES is usually required to find a first-order saddle point where the TS resides. Different automated routines have been developed to efficiently locate transition states; however, for many methods, there is no guarantee that a TS would ever be found.

A highly effective but cumbersome approach is to explicitly calculate a PES by manually varying specific constrained coordinates. In this approach, unconstrained coordinates are allowed to freely relax to minimum energy positions in a standard geometry optimization, and the result is a single data point on a PES surface. After multiple points have been sampled, the PES can be interpolated with minimum curvature or radial basis function algorithms.

The most ubiquitous TS searches use the modified Newton–Raphson routine and start from an atomic configuration close to that of the TS. The optimization procedure successively moves along the normal mode of the Hessian with the lowest magnitude in an attempt to find the point of maximum negative curvature. These methods are rather efficient if the starting geometry is near the real TS and the utilized Hessian contains only one negative mode.[12] When neither of these criteria is applicable, this procedure may fail spectacularly.

Other QM routines incorporate more information either by requiring coordinates from the initial reactant and product configurations or sometimes by including an initial guess for the TS as well. Such routines are quite efficient for locating transition states involving one or two bonds breaking in molecules, but for very large systems such as solids where atom movement influences a larger environment, alternative methods are needed.

For instance, nudge elastic band (NEB) methods are a notable and efficient technique to find these difficult TS without the use of a Hessian. NEB procedures linearly interpolate a series of atomic configurations (the so-called images) aligned in a row between the known initial and final states and then minimize their energies (see Figure 1.3). This method incorporates a limited description of the topology of the PES and thereby reveals the TS as the maximum energy image along the minimum energy reaction path. NEB is not the only procedure that uses a multitude of geometries coupled to each other. However, it is by far one of the most popular means to locate TSs for catalytic reactions happening on surfaces or in bulk environments.

1.2.5.3 Vibrational Frequencies

Vibrational frequencies corresponding to experimental IR spectra are often evaluated only around equilibrium structures (local minima on the PES) using the harmonic oscillator approximation for the potential. Using generalized coordinates[13] for the atom positions Q, Eq. (1.4) becomes

---

12) Diagonalizing the Hessian would lead to a single negative eigenvalue.
13) For example, Cartesian or internal coordinates.
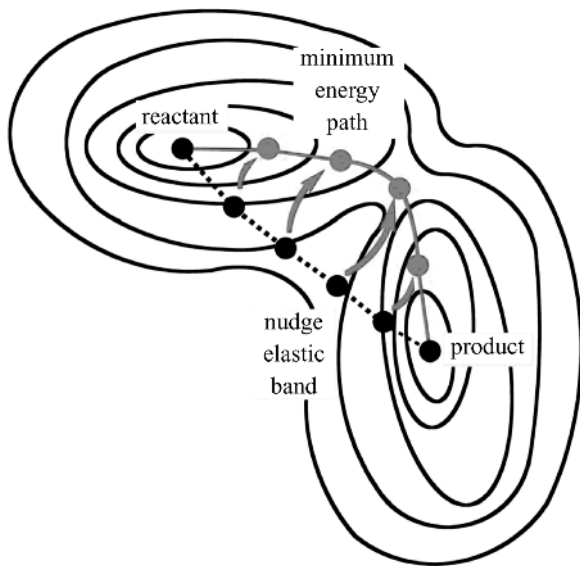
Figure 1.3 Schematic of the NEB method used to find a transition state between reactant and product states.

$$\left[-\sum_{v}^{N} \left(\nabla^2_{Q_v} - \frac{1}{2}\omega_v^2 Q_v^2 \right) \right] \psi_n(Q) = \left(E - E_e(Q^0) \right) \psi_n(Q), \tag{1.46}$$

where $E_e(Q^0)$ is the electronic part of the energy for the system in its equilibrium structure. The quantum mechanical harmonic oscillator problem gives the eigenvalues of previous equations:

$$\left(E - E_e(Q^0) \right)^\kappa_v = \left(\kappa + \frac{1}{2} \right) \hbar\omega_v \tag{1.47}$$

where κ is the vibrational quantum number[14] and ω_v the vibrational frequency along direction v:

$$\omega_v = \sqrt{\frac{k_v}{\mu_v}}, \tag{1.48}$$

with the corresponding force constant k_v and effective mass μ_v. The sign of the force constant shows the curvature of the PES along the particular direction (or mode). Calculated vibrational frequencies are, therefore, often analyzed in order to ensure that a structure optimized to either a stable intermediate or a TS. Indeed, vibrational frequencies should be calculated at the end of every geometry optimization for this very purpose. However, calculated frequencies are not expected to perfectly match

[14] Usually, the index n is used for the quantum number, but this index had already been used to indicate nuclei-related expressions.

with experimental IR frequencies since the previously described approach does not account for anharmonicities of vibrational modes, regardless of the method used.

Equation (1.47) indicates that even in the ground-state $\kappa = 0$ there is a nonzero vibrational contribution to the energy of a system. Energy from this first thermodynamic correction is the zero-point vibrational energy (E_{ZPE}), defined as half of the sum of all vibrational normal modes ω_v:

$$E_{ZPE} = \frac{1}{2} \sum_v \hbar \omega_v. \tag{1.49}$$

1.2.5.4 Thermodynamic Treatments of Molecules

Macroscopic energies based on microscopic contributions can be obtained through traditional statistical thermodynamics using the ideal gas assumption. The rudimentary function that describes macroscopic properties is the partition function, which is separable into electronic, translational, rotational, and vibrational components:

$$E = E_e + E_{trans} + E_{rot} + E_{vib}. \tag{1.50}$$

Each of these energy contributions in turn has internal energy components, U, and entropy, S, which are also separable into components:

$$\begin{aligned} U &= U_e + U_{trans} + U_{rot} + U_{vib}, \\ S &= S_e + S_{trans} + S_{rot} + S_{vib}. \end{aligned} \tag{1.51}$$

We now discuss the different energy and entropy contribution terms as follows:[15]

- **Electronic contributions:** The electronic part of the internal energy U_e can be obtained by solving the electronic part of the many-body problem (Eq. (1.5)). In situations involving electronic degeneracies (i.e., doublet, triplet, and so on states) electronic entropy contributions come into play

$$S_e = k_B \ln(2S + 1), \tag{1.52}$$

  where S is the total spin of the molecular state.
- **Translational contributions:** The temperature-dependent internal energy associated with molecular translations is $(1/2)k_B T$ for every translational degree of freedom of the molecule. In Cartesian space, this leads to $U_{trans} = (3/2)k_B T$. The entropy of translation is

$$S_{trans}^\circ = k_B \left\{ \ln \left[\left(\frac{m_v k_B T}{2\pi\hbar^2} \right)^{3/2} \frac{V^\circ}{N_A} \right] + \frac{5}{2} \right\} \tag{1.53}$$

  where V° is the molar volume of a gas at its standard state: 24.5 ℓ.
- **Rotational contributions:** As for the translational contributions, the temperature-dependent internal energy associated with molecular rotations is also $(1/2)k_B T$

---

15) In this section, all energies are in $k_B T$ (per particle).

for each rotational degree of freedom. While single atoms receive no rotational energy, linear molecules receive $k_B T$, and nonlinear molecules receive $(3/2)k_B T$. The entropy of rotation is

$$S_{\text{rot}} = k_B \left\{ \ln \left[\frac{\sqrt{\pi I_A I_B I_C}}{\sigma} \left(\frac{2k_B T}{\hbar^2} \right)^{3/2} \right] + \frac{3}{2} \right\},$$ (1.54)

where σ is the rotational symmetric number for the molecule's point group, and I_A, I_B, and I_C are the molecule's three principal moments of inertia.

- **Vibrational contributions:** Thermodynamic energy contributions from molecular vibrations are calculated per vibrational frequency, ω_v. Thus, they can be calculated only once vibrational frequencies are obtained from a Hessian calculation. Vibrational energies must be summed over all $3N-6$ molecular vibrations:[16]

$$U_{\text{vib}} = \sum_v \frac{\hbar\omega_v}{e^{\hbar\omega_v/k_B T} - 1}$$ (1.55)

and

$$S_{\text{vib}} = k_B \sum_v \left[\frac{\hbar\omega_v}{k_B T(e^{\hbar\omega_v/k_B T} - 1)} - \ln(1 - e^{-\hbar\omega_v/k_B T}) \right].$$ (1.56)

Using these energy contributions in addition to the calculated E_e from *ab initio* or DFT methods, the following thermocorrected energies can be obtained:

$$H_{0K} = E_e + E_{\text{ZPE}},$$ (1.57)

$$H_T = H_{0K} + U_T \quad (+ k_B T \quad \text{if in gas phase}),$$ (1.58)

$$G_T = H_T - TS_T.$$ (1.59)

1.2.5.5 Considering Solvation

Most chemical processes and catalytic reactions occur in the condensed phase rather than in gas phase. However, including the electronic structure of surrounding molecules implies more complex systems.

The methods used to model solvation can be basically categorized into two main approaches: the explicit and the implicit treatments (see Figure 1.4). In the explicit solvent model (see Refs. [29, 30] for further information), the solvent is described by individual molecules. Consequently, this approach provides detailed information about the structure of the solute/solvent interface for systems near equilibrium and along reaction pathways (e.g., Car–Parrinello *ab initio* molecular dynamics (CPMD) [31]). However, the demands of a purely quantum mechanical treatment requires a system size limited to a relatively small number of solvent molecules.

---

16) For linear molecules, there are $3N-5$ vibrational modes.

(a)

(b)
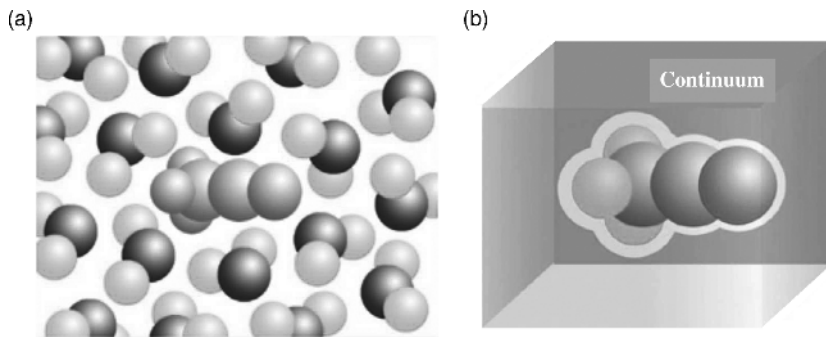
Figure 1.4 Illustrations of solvation methods. (a) Explicit solvation, where solvent molecules (here water) are treated as the molecule of interest. (b) Implicit solvation, where only the molecule of interest is surrounded by a continuum representing the solvent.

An alternative approach is to treat the entire or at least parts of the solvent with a lower level of theory than the solute, for example, with semiempirical force fields [29, 30, 32–34]. In these methods, usually known as QM/MM simulations, the solvent-–solvent, and solute–solvent interactions are mostly given by a sum of electrostatic and van der Waals contributions. Further, the coupling between the quantum-mechanically treated solute and the molecular-mechanically treated solvent needs particular attention. Possible solutions are provided by a multipolar expansion of the QM wave functions [35, 36] or a solvent-averaged potential.

Much less demanding implicit solvent approaches [37, 38] can provide a useful correction accounting for solvation. These methods use a continuous electric field to represent a statistical average of the dielectric effects of the solvent over all the solvent degrees of freedom. The solute is then placed in a cavity, whose size and shape have to be chosen properly. Different ways exist to define these cavities, for example, using atom-centered interlocked spheres of certain radii [37, 39], the solvent-excluded surface (SES) [40], or the solvent-accessible surface (SAS) [41] method. Due to electrostatic interactions, the solute polarizes the solvent, which then forms the so-called reaction field that couples back to the solute. The corresponding electrostatic potential, which is required to evaluate the interaction energy, is obtained by solving the Poisson–Boltzmann equation (assuming a Boltzmann-type distribution of ions within the solvent):

$$\nabla[\varepsilon(\mathbf{r})\nabla V_{es}(\mathbf{r})] = -4\pi\left[\varrho^f(\mathbf{r}) + \sum_i c_i^\infty z_i \lambda(\mathbf{r}) e^{-z_i V_{es}(\mathbf{r})/k_B T}\right], \tag{1.60}$$

where $\varepsilon(\mathbf{r})$ is the position-dependent dielectric, V_{es} is the electrostatic potential, ϱ^f is the charge density of the solute, c_i^∞ is the bulk concentration of ion-type i with the net charge z_i, and finally $\lambda(\mathbf{r})$ is a factor for the position-dependent accessibility of the solution to position $\mathbf{r}$. This leads to a contribution to the overall free energy of a system:

$$\Delta G^{solv} = \Delta G^{chg} + \Delta G^{cav}, \tag{1.61}$$

where the two terms account for the free energy to generate the cavity and for charging the solvent near the solute.

In quantum mechanical calculations of a solute electronic structure, the solvent reaction field is incorporated into the iterative cycle, resulting in the so-called self-consistent reaction field (SCRF) approach. Instead of solving the Poisson–Boltzmann equation directly, different approximations exist to evaluate the solvation free energy by analytic expressions, for instance, the generalized Born model [42, 43], the Bell model, or the Onsager model [37, 38].

1.2.6
Model Representation

Studying surface-specific problems such as structures, adsorptions, and catalytic reactions is a formidable task and requires one of the two surface model approaches: the periodic slab/supercell approach and the cluster approximation. Both models have advantages and disadvantages. The choice depends on the particular physical or chemical question to be answered.

1.2.6.1 Slab/Supercell Approach
Although the many-body problem has been simplified by the formulation of DFT, calculating the electronic structure of extended systems (e.g., bulk, surfaces, and chains) with infinite number of electrons (e.g., in a solid) is of course impossible. However, by assuming periodic boundary conditions and applying Bloch's theorem [44], the calculation of extended systems becomes possible.

The Bloch theorem states that each electronic wave function[17] in a periodic solid can be written as the product of a periodic function, $u_{n,\mathbf{k}}(\mathbf{r})$, and a plane wave, leading to

$$\phi_{n,\mathbf{k}} = u_{n,\mathbf{k}}(\mathbf{r})e^{i\mathbf{k}\cdot\mathbf{r}}, \tag{1.62}$$

where $\mathbf{k}$ is the wave vector that lies inside the first Brillouin zone (BZ). The index n, the band index, labels the wave functions for a given $\mathbf{k}$. The function $u_{n,\mathbf{k}}(\mathbf{r})$ has the periodicity of the supercell and can be expanded using a set of plane waves

$$u_{n,\mathbf{k}}(\mathbf{r}) = \sum_{\mathbf{G}} c_{n,\mathbf{k}}(G)e^{i\mathbf{G}\cdot\mathbf{r}}, \tag{1.63}$$

where the wave vectors $\mathbf{G}$ are reciprocal lattice vectors fulfilling the boundary condition of the unit cell, $\mathbf{G}\cdot\mathbf{L} = 2\pi\nu$.

The physical quantities of a system, such as the electron density and total energy, are obtained by performing an integration into reciprocal space. Numerically, the integral over the BZ can be transformed into a sum over only a finite number of $\mathbf{k}$-points, called the $\mathbf{k}$-point mesh:

---

17) Here, we show derivation for the density functional theory, thus expanding Kohn–Sham orbitals. However, the Bloch theorem is not restricted to DFT.

(a)

Unitcell

(b)
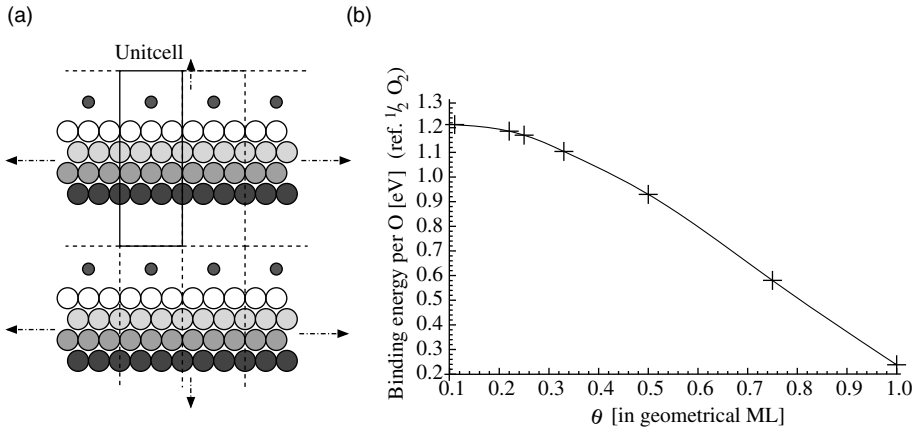
Figure 1.5 (a) Illustration of the supercell approach for surface calculations. The periodically repeated unit cell (2D slab) has to be large enough to minimize interactions with neighboring unit cells. (b) Binding energy of an oxygen atom as a function of surface coverage (with gas-phase 1/2 O_2 as reference).

$$\int_{\mathrm{BZ}} \frac{1}{\Omega_{\mathrm{BZ}}} \mathrm{d}\mathbf{k} \rightarrow \sum_{\mathbf{k}} \omega_{\mathbf{k}}. \tag{1.64}$$

The error introduced by this approximation can be minimized if a sufficiently dense set of **k**-points is used, but the computational effort grows quickly with the number of **k**-points. Therefore, it is crucial to test the convergence of the results with respect to the number of **k**-points and choose an appropriate mesh size.[18]

In principle, an exact representation of the electronic wave functions should require an infinite number of plane waves. In practice, however, a finite number of plane waves up to a certain cutoff, E_{cutoff}, already provides sufficiently accurate results:[19]

$$\frac{1}{2}|k+G|^2 \leq E_{\mathrm{cutoff}}. \tag{1.65}$$

Periodic systems are modeled by concentrating on the smallest possible unit cell and periodically repeating it over all space. For bulk materials, this box of atoms is mostly set up by using the primitive unit cell of the crystal. For a surface, however, the periodicity in direction perpendicular to the surface is broken. Surfaces are modeled by a periodic 3D structure containing crystal slabs separated by vacuum regions (see Figure 1.5) in order to maintain the periodicity in this direction. This so-called supercell approach represents the surfaces periodically, and they must be separated

---

18) Different schemes have been proposed to distribute the **k**-points within the unit cell. The commonly employed scheme of a homogeneous grid of **k**-points was introduced by Monkhorst and Pack [45].

19) In practical calculation, the cutoff energy is obtained by carefully checking the convergence of system properties with respect to the cutoff value.

by a vacuum wide enough to avoid unwanted interactions between slabs and their virtual copies above and below. Furthermore, the slab must be thick enough so that its center reproduces bulk-like behavior to avoid unphysical interactions between the surfaces on the top and the bottom of the slab. Depending on the system, this requires between 5 and sometimes even more than 20 atomic layers. Semiconductors and certain transition metals exhibit major surface properties, such as surface states or adsorbate binding energies, with only five-layer slabs. Some simple metals (e.g., Al) require more layers.

If the aim is to study catalytic reactions on surfaces, modifying the lateral extension of the unit cell also allows investigation of coverage effects. The zero-coverage limit requires rather extended unit cells to ensure that adsorbed species interact neither directly with their images in adjacent cells nor indirectly through changes in the electronic structure of the surface. Figure 1.5a shows the DFT-calculated binding energy of a single oxygen atom (with respect to half an O_2 molecule) on a face-centered cubic (fcc) site of a Pt(111) slab as a function of unit cell size (or coverage). Here, negligible adsorbate–adsorbate interactions are received with a 3×3 unit cell.

1.2.6.2 Cluster Approach

When simulating finite systems such as molecules or clusters, the cluster approach is more suitable. In particular cases, even surfaces can be modeled as cluster where a finite segment of the surface models the extended system (see Figure 1.6). Despite the lack of periodicity in this approach, the finite system avoids most issues connected with direct and indirect interactions of nearby slab images.

When modeling metallic surfaces with small clusters, most (if not all) atoms may be surface atoms. This causes unwanted border effects and an unpredictable behavior of the cluster that is why such clusters have to be built with special care. The graph in Figure 1.6b shows calculated binding energies for atomic oxygen (again
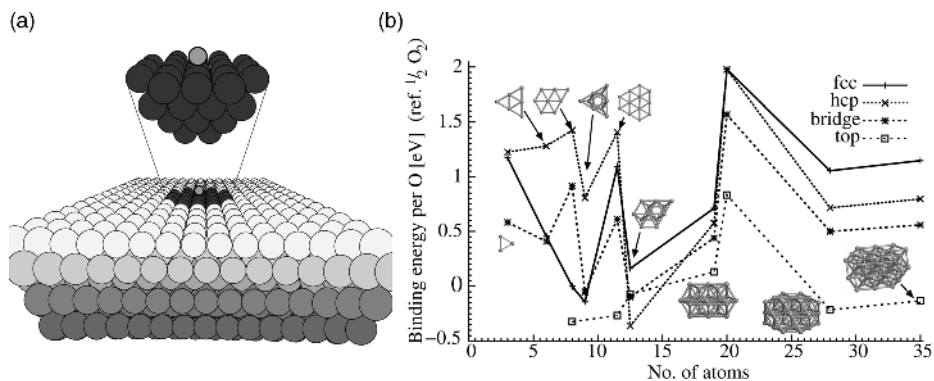
Figure 1.6 (a) A well-defined, finite cluster is used to model the surface in the cluster approach. (b) Binding energies (with respect to gas-phase 1/2 O_2) of atomic oxygen on differently sized and shaped clusters (Pt_3, Pt_6, Pt_8, Pt_{12}, $Pt_{6.3}$, $Pt_{12.8}$, $Pt_{5.10.5}$, $Pt_{9.10.9}$, $Pt_{14.13.8}$). For each cluster, the binding energies at fcc, hcp, bridge, and on-top sites are given.

with half an O_2 molecule as reference) on the (111) plane of differently sized and shaped Pt clusters [46].

On clusters of fewer than 20 atoms, the atomic oxygen binding energy and preferred adsorption site strongly depend on the system. Extending the cluster to more than 20 atoms results in a concordance of preferred adsorption sites and similar relative stabilities. However, convergence in binding energy and adsorption structure requires clusters of at least 3 atomic layers and 28 atoms. When such large clusters are used, calculated binding energies agree quite well with periodic calculations at low adsorbate coverages. Other metal surfaces sometimes require even more extended systems (e.g., 56 atoms for Cu(100) [47] or >100 atoms for Al(100) [48]). Although finite systems can mimic surfaces, systematic studies on cluster size convergence are necessary.

1.3
The Electrocatalytic Oxygen Reduction Reaction on Pt(111)

The ORR is a canonical chemical reaction due to its ubiquitous presence in corrosion, combustion, energy conversion, and storage processes. After describing the different aspects of the theoretical modeling of catalytic reactions, we now show how to apply these concepts to understand one of the most fundamental reactions in electrocatalysis. Besides its importance in basic electrochemistry, the oxygen reduction reaction is also relevant to energy conversion in polymer electrolyte membrane fuel cells (PEM-FCs).

In principle, gaseous H_2 is oxidized at the anode and its protons migrate through the electrolyte to the cathode where they finally react with O_2 under uptake of four electrons to form two water molecules.

Despite the apparently simple reaction mechanism shown in Table 1.1, the exact reaction mechanism and thus the fundamental reaction steps of the ORR are still not fully understood. Indeed, this reaction is highly complex since it occurs in a multicomponent environment and is influenced by various environmental parameters: temperature, pressure, and electrode potential.

Before discussing the electrochemical ORR, we will investigate the Pt-catalyzed water formation out of gaseous O_2 and H_2, which is the closest surface science analogue to the ORR. After this, the generalization to electrocatalysis will be undertaken, for which only a few additional processes have to be included.

Table 1.1 The oxygen reduction reaction potentials.

Anode :	$2H_2$	$\rightarrow$	$4H^+ + 4e^-$	$E^\circ = 0\,\text{V}$
Cathode :	$O_2 + 4H^+ + 4e^-$	$\rightarrow$	$2H_2O$	$E^\circ = 1.229\,\text{V}$
Net :	$2H_2 + O_2$	$\rightarrow$	$2H_2O$	$E^\circ = 1.229\,\text{V}$
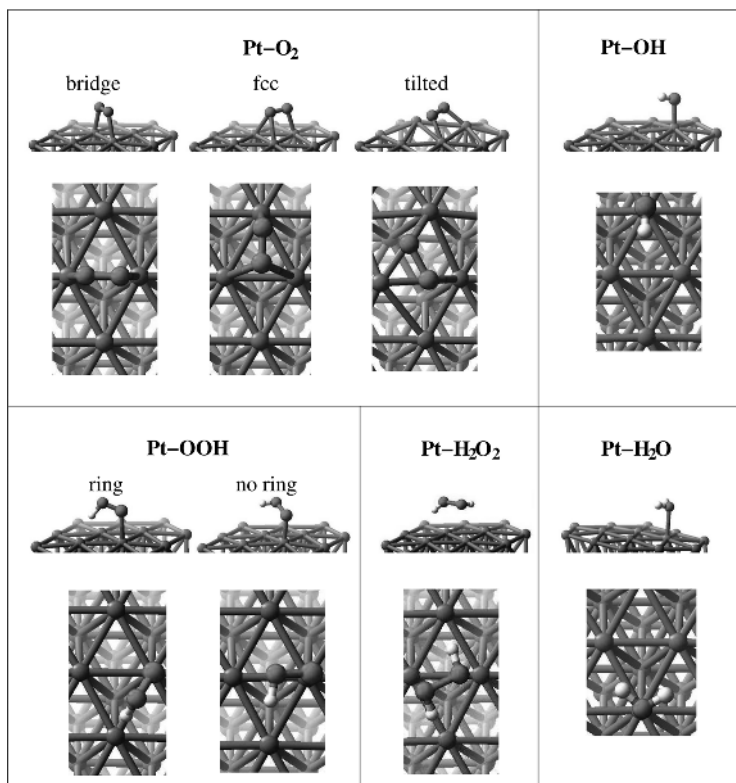
Figure 1.7 Side and top views of the different molecules adsorbed on Pt(111).

The fundamental steps for both surface science water formation and electrochemical ORR were calculated with DFT.[20] We considered adsorbed and nonadsorbed binding energies for all possible intermediates separately: H, H_2, O, O_2, OH, OOH, H_2O_2, and H_2O. We determined stable surface sites and binding energies for each intermediate on Pt(111) (see Figure 1.7). We then calculated barriers for all adsorbed molecule dissociation processes [50, 51]. We optimized transition states by a series of constrained optimizations along their reaction paths. Table 1.2 summarizes the corresponding binding energies and dissociation barriers. This includes values for the systems in gas phase, solvated in water, and finally under ambient conditions, that is, free energies at $T = 298$ K.

20) DFT calculations on the water formation mechanisms used the Jaguar code [49] spin restricted density DFT with the B3LYP gradient-corrected exchange–correlation functional and included zero-point energy (ZPE) corrections and implicit solvation when noted. The 60 core electrons in each Pt atom (1s-4f) were treated with the Hay and Wadt core-valencer elativistic effective core potential (ECP), leaving 18 valence electrons to be treated with the LACVP** basis set. The other elements (H and O) were described with the all-electron 6-31G** basis set. To represent the Pt(111), a 35-atom Pt cluster was used, which ensured cluster-size converged energies.

Table 1.2 Calculated binding energies and dissociation barriers for all investigated intermediates.

System	Adsorption site	Binding energies (eV)			Bond	Dissociation energies (eV)		
		ΔE^{gas}	ΔE^{solv}	ΔG^{solv}_{298K}		ΔE^{gas}	ΔE^{solv}	ΔG^{solv}_{298K}
$H_2^{g,aq}$	—	—	—	—		4.84	4.81	4.22
$O_2^{g,aq}$	—	—	—	—		4.95	5.46	5.05
$OH^{g,aq}$	—	—	—	—		4.57	4.83	4.31
$OOH^{g,aq}$	—	—	—	—	OO$-$H	2.79	2.69	2.12
	—	—	—	—	O$-$OH	3.17	3.32	2.86
$HOOH^{g,aq}$	—	—	—	—	HOO$-$H	3.83	4.00	3.44
	—	—	—	—	HO$-$OH	2.43	2.48	1.99
$H_2O^{g,aq}$	—	—	—	—		5.24	5.39	4.57
Pt$-$H	Top	2.73	3.09	2.67		—	—	—
	Bridge	2.64	3.43	3.07		—	—	—
Pt$-$O	fcc	3.24	4.40	4.04		—	—	—
	hcp	3.03	—	—		—	—	—
Pt$-$O$_2$	Bridge	0.49	1.31	0.81		1.34	0.81	0.90
	fcc	0.31	1.64	1.15		1.03	1.11	1.19
	Tilted	0.06	0.85	0.36		0.22	−0.10	−0.11
Pt$-$OH	Top	2.06	3.03	2.61		1.90	1.15	0.99
Pt$-$OOH	No ring	1.03	2.18	1.57	OO$-$H	1.03	0.72	0.57
	Ring	0.75	2.07	1.37	O$-$OH	0.74	0.62	0.59
					OO$-$H	0.36	0.81	0.71
Pt$-$HOOH	Bridge	0.41	1.36	0.52	HOO$-$H	0.94	0.96	0.78
					HO$-$OH	0.46	0.43	0.31
Pt$-$H$_2$O	Top	0.60	0.83	0.56		1.29	0.86	0.73

Energies are given for the compounds in gas-phase, solvated in water, and under ambient conditions (including thermal corrections).

This data affords a picture of different pathways (see Figure 1.8). In general, three major pathways are readily distinguishable. First, O_2^{ad} can dissociate on the surface generating two O^{ad} atoms and then react with H^{ad} atoms to form water. Second, the O_2^{ad} molecule can react with hydrogen to first form OOH^{ad} or then form $HOOH^{ad}$. After the O$-$O bond in these species breaks, the remaining species further reacts to the final product water. All pathways appear to be strongly influenced by the presence of the electrolyte.

1.3.1
Water Formation from Gaseous O$_2$ and H$_2$

Since many reactions and concepts of heterogeneous catalysis in surface science have analogues in electrocatalysis, we first discuss the Pt-catalyzed water formation from gaseous hydrogen and oxygen. The three major reaction pathways are separately described, and then we draw general conclusions on the overall mechanism.
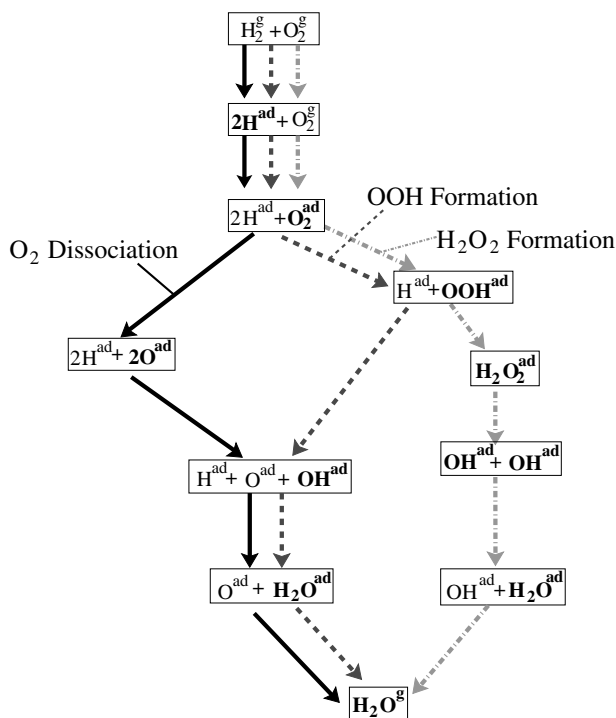
Figure 1.8 Schematic showing three main reaction pathways for the formation of water out of gaseous H_2 and O_2.

1.3.1.1 **O_2 Dissociation**

When O_2 adsorbs on the Pt(111) surface, three stable binding geometries are found: bridge ($BE = 0.49$ eV), fcc ($BE = 0.31$ eV), and tilted ($BE = 0.06$ eV) (see Figure 1.7). The most stable configuration is O_2^{ad} bound at a bridge position, where both oxygens use a doubly occupied *p*-orbital to form donor–acceptor bonds to the surface. The second stable structure corresponds to dioxygen above a fcc[21] surface-site, such that one oxygen binds on top of a Pt atom and the other oxygen at a bridge position. Finally, the last structure is somewhat comparable to bridge-bound O_2^{ad}, except that the molecule is tilted toward the surface such that the $O=O$ π bond can form a donor–acceptor bond to an adjacent Pt atom.

After adsorption, O_2^{ad} may dissociate with one of the three dissociation barriers corresponding to those from the bridge (1.34 eV), the fcc (1.03 eV), or the tilted configuration (0.22 eV). Although, tilted O_2 forms the weakest surface bond, this adsorbate structure has the lowest dissociation barrier. Binding energy alone suggests that O_2^{ad} resides at a bridge surface site. However, the tilted configuration is 0.90 eV lower than the bridge-site dissociation barrier. Thus, O_2^{ad} may change its

---

21) The fcc-site is a threefold position where there is no Pt atom in the second layer below.

structure to the tilted configuration (which does not require much reorganization) and then dissociate via the O_2-tilted route. By doing so, the overall dissociation barrier reduces from 1.34 eV to only 0.65 eV, which is in much better agreement with the value of 0.38 eV measured by Ho and coworkers [52].

The products of O_2^{ad} dissociation are two O^{ad} atoms located in threefold sites: O_{fcc}/O_{fcc}, O_{hcp}/O_{hcp}, or O_{fcc}/O_{hcp}. Our simulations show dissociation results in two O^{ad} atoms at nonadjacent threefold positions (separated by two lattice constants), also in excellent agreement with the scanning tunneling microscopy (STM) experiments by Ho [53, 54]. When multiple O_2^{ad} dissociations are considered to occur across the entire surface, the final structure corresponds to a $p(2 \times 2)$ overlayer, a result we also obtained by evaluating the surface phase diagram of various adlayer configurations [55, 56] and which had also been observed experimentally [57]. Since the O−O interactions are already rather small, for coverages ≤ 0.25 ML it is justified to simulate O^{ad} atoms as independent adsorbates. Therefore, we neglected coverage effects in our simulations. The barrier to hop from a hexagonal close packed (hcp) to a fcc site via a bridge position is only 0.24 eV, so we expect most atomic oxygen will eventually migrate to the most thermodynamically stable fcc sites.

The next reaction step along the O_2 dissociation pathway is the formation of OH^{ad}, a process whose barrier is 1.25 eV. In contrast to O_2^{ad} dissociation, no alternative trajectory with a lower dissociation barrier was found. This process leads to adsorbed but mobile H^{ad}, partially hcp-bound O_{fcc}^{ad}, and OH^{ad}. Hydrogenation of OH^{ad} leads to a water molecule that can then desorb as a gas-phase water, the final product of the ORR reaction. Both H_2O^{ad} and OH^{ad} adsorb on Pt(111) with their oxygens at on-top surface sites. The binding energy to form H_2O^{ad} from OH^{ad} and H^{ad} is the sum of breaking the Pt−OH covalent bond (2.06 eV), forming the Pt−OH_2 donor–acceptor bond (−0.60 eV), breaking the surface Pt−H bond (2.73 eV), and forming the OH−H bond (−5.24 eV). This leads to a lowering of the system energy by −1.05 eV. The barrier connected with the water formation out of OH^{ad} and H^{ad} is only 0.24 eV. Finally, water desorption requires breaking the Pt−H_2O surface bond (0.60 eV), a value comparable to the experimental value of 0.52 eV [58].

The complete O_2 dissociation pathway in gas phase is shown in Figure 1.9. Energies reported so far *do not* include zero-point energy corrections or thermal contributions, thus represent the case of 0 K temperature. All reaction steps are exothermic except water desorption from the surface. The overall calculated reaction enthalpy at 0 K is 2.50 eV (per water molecule), a value comparable to the Nernst equation enthalpy value[22] of 2.46 eV. However, the latter value is under ambient conditions and includes the electrolyte effects we will discuss in later sections.

Only three steps of this entire process have barriers. The highest barrier (1.25 eV) is the $O_{fcc}^{ad} + H^{ad} \rightarrow OH^{ad}$ reaction. Dissociation of O_2^{gas} in the absence of the heterogeneous Pt catalyst is 4.92 eV, but dissociation of O_2^{ad}, usually considered the rate-determining process for the ORR reaction, is 0.65 eV. The last reaction barrier

---

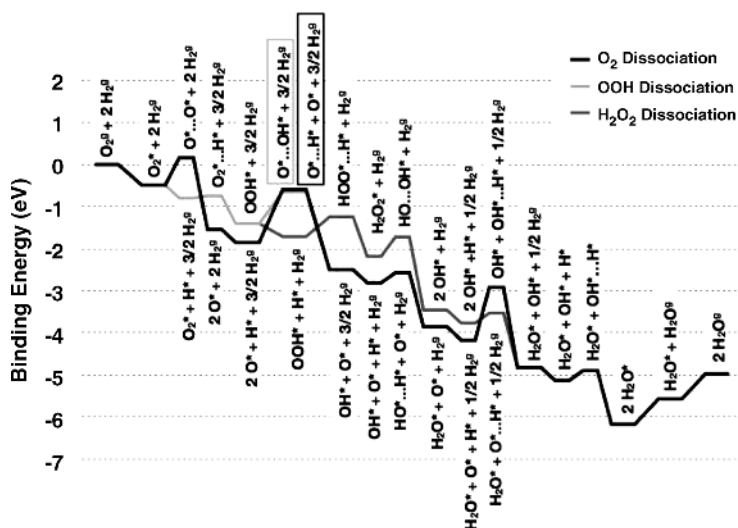22) Two electrons are transferred: $2e \times 1.23 V = 2.46$ eV.

Figure 1.9 Gas-phase Langmuir–Hinshelwood reactions.

(0.24 eV) is formation of water on the surface from $OH^{ad} + H^{ad}$. This calculation data supports that the rate-determining step (RDS) should be the OH^{ad} formation. Experimental values for the overall ORR activation range from 0.1 to 1.0 eV; however, the value also depends on the experimental system and measurement conditions [59]. The discrepancy between our calculated barrier indicates that this reaction process may not be a relevant mechanism for the ORR.

1.3.1.2 OOH Formation

Instead of dissociating after adsorption, O_2^{ad} might first undergo a hydrogenation step to form adsorbed OOH^{ad}, which then may dissociate to form OH^{ad} and O^{ad}. As in the O_2 dissociation pathway discussed in the previous section, the generated OH^{ad} molecule could then react with another H^{ad} to from water, which finally desorbs from the surface. The energies along this OOH formation pathway have also been added to the diagram shown in Figure 1.9.

As adsorbed hydrogen is extremely mobile on the Pt(111) surface,[23] several different processes for the OOH formation mechanism should be considered. H^{ad} could approach O_2^{ad} roughly perpendicular to the O−O direction and then bind to an oxygen. Electronic rearrangement from an O−O π bond to the stronger O−H σ bond causes the other O atom to form a stronger covalent surface connection.

The barrier to form OOH^{ad} along this process is 0.43 eV. However, when H^{ad} approaches O_2^{ad} along the Pt–Pt bridge direction, another stable OOH^{ad} structure forms, in which OOH^{ad} and two surface Pt atoms form a five-membered ring structure. A strong Pt–H interaction weakens the adjacent Pt–O donor–acceptor bond, resulting in a 0.38 eV lower barrier for the $H^{ad} + O_2^{ad} \rightarrow OOH^{ad}$ process. The

---

23) Binding energies at different surface sites vary only by < 0.10 eV.

ring structure is unstable and can easily tautomerize into the nonring OOH^{ad} structure (see Figure 1.7). Therefore, we consider only the nonring OOH^{ad} structure as relevant.

Once adsorbed OOH has been formed, dissociation to OH^{ad} + O^{ad} has a barrier of 0.74 eV. The products are OH^{ad} at an on-top site and O^{ad} in a threefold site. The O$-$OH bond breaks along the O$-$O direction, and the single O atom must migrate over a top site before moving into its preferred threefold site. Along the dissociation, there is no calculated preference for O^{ad} to move into an adjacent fcc or hcp site. However, as discussed in the previous section, O^{ad} at an hcp position should easily migrate over a bridge position (0.24 eV barrier) to a fcc site. Finally, water formation and water desorption steps are the same as those described in the previous section.

Just like the O$_2^{ad}$ dissociation mechanism, every step of the OOH formation pathway is exothermic except for the last reaction step, that is, desorption of water. The OOH^{ad} mechanism involves three activation barriers: formation of OOH^{ad} (0.05 eV), the dissociation of an oxygen from OOH^{ad} (0.74 eV), and the final water surface desorption (0.24 eV). Thus, we find the O$-$OH dissociation is rate determining for the OOH^{ad} formation pathway, and due to an overall lower energy barrier it is a likelier ORR mechanism than the O$_2^{ad}$ dissociation (at least under gas-phase conditions).

### 1.3.1.3 HOOH Formation

The third mechanism considers OOH^{ad} undergoing another hydrogenation step to form HOOH^{ad} on the surface with an energy barrier of 0.47 eV. Two OH^{ad} adsorbates then form after HO$-$OH bond dissociation (0.46 eV). The remaining intermediates have already been discussed in the previous section. The highest barrier along the HOOH^{ad} pathway is the formation of HOOH^{ad} in gas phase (0.47 eV), thus being the rate-determining step. Consequently, the barrier for the RDS along the H$_2$O$_2$ formation pathway is 0.26 eV below the RDS of the OOH formation and 0.51 eV lower than that of the O$_2$ dissociation mechanism. Both the OOH formation and the HOOH formation pathways, which have energy barriers for the RDS of 0.74 eV and 0.47 eV, respectively, now show a much better agreement with experimental observations than the O$_2$ dissociation with an RDS barrier of 1.25 eV. Drawing this conclusion was possible only after investigating all three mechanisms individually. Furthermore, we have not yet included solvation or thermal effects, and either might certainly influence overall reaction kinetics. Therefore, we now will repeat the previous studies in the presence of water, which is the main constituent of the electrolyte.

1.3.2
Simulations Including Water Solvation

Electrocatalysis involves surface reactions under wet conditions. Compared to the gas-phase water formation, which had been discussed in the previous section, inclusion of an electrolyte will certainly alter energetics along the ORR and may even modify the preferred reaction mechanism. Besides these purely electronic

Langmuir–Hinshelwood
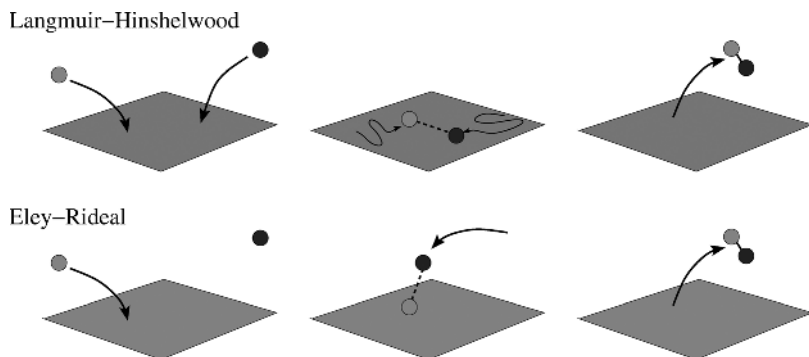
Eley–Rideal

Figure 1.10 Schematic showing the Langmuir–Hinshelwood (*top*) and the Eley–Rideal (*bottom*) reaction mechanism.

effects, the solvent may also play an explicit role in the reaction steps. Therefore, two classes of reactions should be considered when an electrolyte is present. Besides Langmuir–Hinshelwood reactions, which have already been presented, Eley–Rideal reaction mechanisms rely on the electrolyte as a source of hydrogen atoms (see Figure 1.10).

We already mentioned that solvation presents a formidable problem for theory. Although results from gas-phase calculations are sometimes used to interpret experiments performed in solution, we believe that at least some treatment of the water solvent is required to obtain relevant results. Full quantum mechanics simulations alone would not provide completely accurate comparisons to experimental observations, but molecular dynamics simulations updated with quantum chemical forces (via *ab initio* molecular dynamics) usually provide reliable accuracy relevant to extended timescales. Unfortunately, the scaling of such methods quickly makes simulations too large and complex to simulate, especially for those with many intermediates and barriers such as the ORR reaction. As described in Section 2.5.5, an alternative approach is to treat solvation using a dielectric continuum. Although this method lacks dynamical information, qualitatively correct electrostatic behavior is attainable.

A self-consistent reaction field description of the water solvent augmented our studies on the ORR reactions. The binding energies and reaction barriers of the previous mechanisms were recalculated in the presence of water environment and used to generate Figure 1.11. Comparing gas-phase results to solvated results often shows large stabilizations of adsorbed species. Large stabilizations are certainly due to a partial charge transfer between the adsorbate and the surface, which was not observable without a polarizing environment. This results in a positive partial charge ($\delta+$) for each hydrogen and a slight negative partial charge ($\delta-$) for each oxygen. These charges interact with the water dipoles, polarizing the solvent, and thus further stabilize adsorbates.

We will now first discuss Langmuir–Hinshelwood-type reactions, describing the main electronic effects introduced by the water environment, and then consider
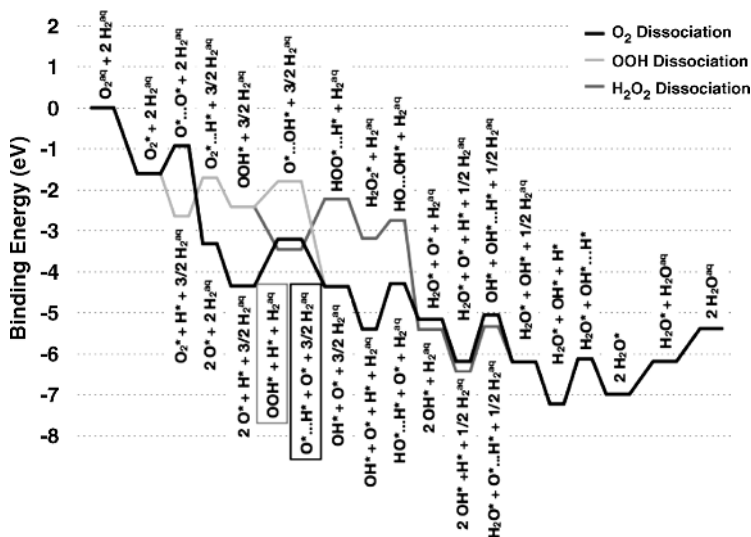
Figure 1.11 Langmuir–Hinshelwood reactions in water solvent.

Eley–Rideal-type reactions, where the protonations occur from the electrolyte directly.

1.3.2.1 Langmuir–Hinshelwood Mechanisms

- **O$_2$ Dissociation:** O$_2^{ad}$ dissociation leads to two O^{ad}, which is now -1.71 eV downhill in solvent (water) rather than -1.05 eV in gas phase. The barrier for this dissociation, however, hardly changes from 0.65 to 0.68 eV. As mentioned before, this is certainly due to the higher degree of polarization of O^{ad} compared to O$_2^{ad}$. After dissociation of O$_2^{ad}$, O^{ad} reacts with a surface hydrogen to form OH^{ad}. Now, the reactants and products in this reaction are isoenergetic, instead of products being favored by 0.65 eV in gas phase. The barrier to form OH^{ad} drops from 1.25 eV in gas phase to 1.14 eV in solution. We observe a similar barrier (1.10 eV) to form H$_2$O^{ad}; however, this barrier was 0.24 eV in gas phase. Despite these changes, water solvation causes little change to the overall O$_2^{ad}$ dissociation pathway. We find that the formation of OH^{ad} is still the rate-determining step for this mechanism, but this again does not conform to experimental expectations [60]. Water desorption from the solvated surface requires 0.83 eV, a value that is comparable to the binding energy of a water molecule within an entire water bilayer network.[24] This shows that application of an SCRF model in surface catalysis simulations is a relatively inexpensive approach to reproduce the qualitative behavior from experiment.

---

24) In the bilayer network, the Pt–H$_2$O bond energy is 0.38 eV, and the two hydrogen bonds bring 0.28 eV each. In total, removing H$_2$O^{ad} from a water bilayer network on top of the Pt(111) surface requires 0.94 eV [61–64].

- **OOH Formation:** For the OOH^{ad} formation pathway, the initial steps are again equivalent to the O_2 dissociation, but OOH^{ad} formation is now 0.22 eV *uphill* in water solvent compared to -0.60 eV *downhill* in gas phase. The OOH^{ad} formation barrier is greatly increased from 0.05 eV in gas phase to 0.94 eV in solvent. The solvent substantially destabilizes both the transition state and OOH^{ad}. Water has a small effect on the dissociation of OOH^{ad} (0.74 eV in gas phase and 0.62 eV in solvent). This reaction step is exothermic by -1.94 eV, which is -0.84 eV lower than in gas phase. Here again, OOH^{ad} formation should be the rate-determining process for this mechanism.
- **HOOH Formation:** Just as the OOH^{ad} formation step was heavily influenced by solvation, so is the $HOOH^{ad}$ formation step. $HOOH^{ad}$ formation in gas phase had a barrier of 0.47 eV, which increases to 1.23 eV in solvent. Similarly, due to the minor charge transfer between $HOOH^{ad}$ and the Pt surface, HO$-$OH dissociation is hardly affected by solvation just as O$-$OH was not (gas-phase barrier $=$ 0.46 eV; solvent-phase barrier $=$ 0.43 eV). Overall, $HOOH^{ad}$ formation is the RDS for this mechanism.

Overall Langmuir–Hinshelwood reaction mechanisms appear to be drastically influenced by solvation effects, particularly when H^{ad} reacts with another adsorbate. In gas phase, we found that $HOOH^{ad}$ formation has the lowest barriers, thus being the overall RDS (0.47 eV). In solvent, OOH^{ad} formation is the overall RDS (0.62 eV), and $HOOH^{ad}$ formation is unfavorable. The key energy barriers of these ORR mechanisms (O_2^{ad} dissociations, OOH^{ad} formation, and $HOOH^{ad}$ formation) are influenced by solvent as much as 0.89 eV, greatly altering interpretations from available literature data on the ORR activation energy [59]. In summary, by including the electronic effects of the surrounding water solution, we found a preference against $HOOH^{ad}$ formation; however, both the O_2^{ad} dissociation and the OOH^{ad} formation reactions should be competitive under these simulation conditions. Therefore, compared to the gas-phase system, considering the water environment not only changed the energies and barriers but also led to a different reaction mechanism to be favorable.

1.3.2.2 Eley–Rideal Reactions

Eley–Rideal mechanisms are surface reactions where a surface intermediate reacts with the solvent. In terms of the ORR, Eley–Rideal mechanisms involve hydrogenations from protons in the electrolyte. We use the initial thermodynamic resting state of hydrogen gas in solution as referenced to hydrogen gas out of convenience. This reference eschews problems and complexity with treating the electronic structure or protons in aqueous solution, an especially problematic simulation for theoretical methods. Indeed, a rigorous simulation for a full electrochemical system should consider a kinetic chemical equilibrium between H^{ad} and H^+; however, thermodynamic energies can still be reported. In Eley–Rideal mechanisms, hydrogen enters the simulation in the transition state for the hydrogenation process. Intermediates found in Langmuir–Hinshelwood mechanisms are exactly the same.
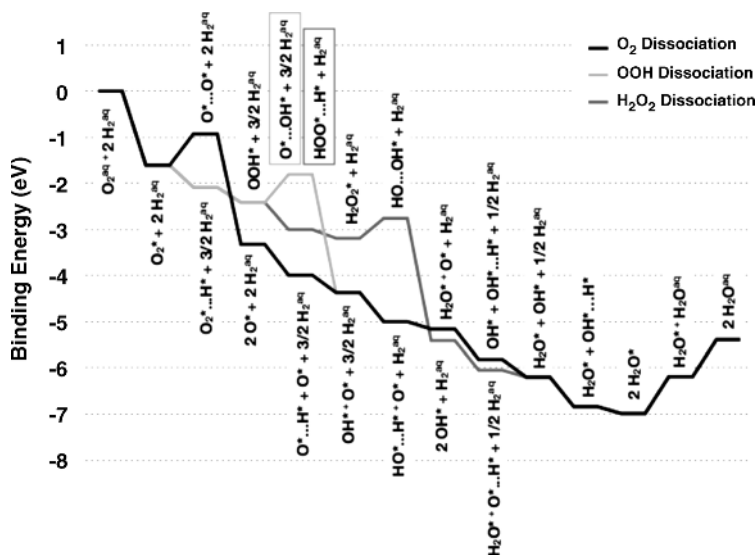
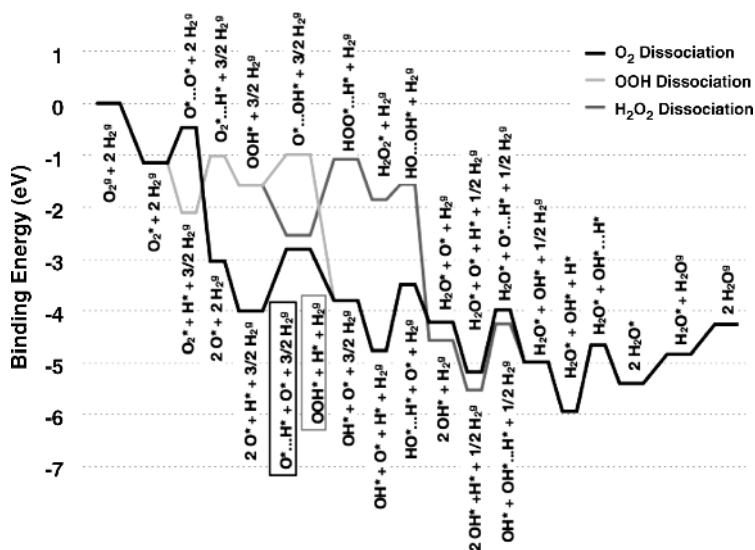**Figure 1.12** Eley–Rideal-type reactions in water solvent.

Simulations on the dissociation steps of O_2^{ad}, OOH^{ad}, and $HOOH^{ad}$ provide substantially different reaction details than those previously reported, where protons from the electrolyte first adsorb on the surface and then further react as H^{ad}. The rate-determining step for O_2^{ad} dissociation in solvent phase was OH^{ad} formation (1.14 eV); however, in an Eley–Rideal-type mechanism, this process has no barrier partly due to its reference at the highly acidic standard state (pH = 0) of the electrolyte, whereby protons should rapidly and easily protonate O^{ad} species. Thus, the resulting RDS of the O_2^{ad} dissociation pathway now becomes the dissociation of O_2^{ad} itself (0.68 eV), which agrees with the expectations from electrochemistry. For the OOH^{ad} formation pathway, the RDS still remains to be the O−OH dissociation (0.62 eV), and for the $HOOH^{ad}$ formation pathway also the HO−OH dissociation stays to be the RDS (0.43 eV). Overall, treatment of Eley–Rideal mechanisms shows that all three pathways are potential candidates to be possible reaction mechanisms for the ORR, with a slight preference for the $HOOH^{ad}$ formation pathway at zero potential (0.0 V). These results are summarized in Figure 1.12.

1.3.3
Including Thermodynamical Quantities

As we had shown in Section 2.5, quantum mechanical electronic energies alone should not be compared with experimental observables taken from measurements on macroscopic systems under ambient conditions. Zero-point energies and free energy contributions must be added to electronic energies of the solvated system. We use first-order approximations for these values obtained from statistical thermodynamics and the ideal gas approximation at room temperature $T = 298$ K.

Figure 1.13 Langmuir–Hinshelwood reactions in water solvent under ambient conditions (including thermal contributions for $T = 298$ K).

1.3.3.1 Langmuir–Hinshelwood and Eley–Rideal Mechanisms

As expected, we do not find many notable differences due to free energy contributions in terms of barrier heights. However, we find that free energy contributions indeed make a very large difference when accounting for water formation at the end of the ORR reactions. In gas phase, the overall ORR reaction is exothermic by -5.00 eV (without E_{ZPE} corrections). In solvent, this value is even more exothermic, -5.36 eV. Including free energy contributions brings this value back even higher than the gas phase value, -4.65 eV. Thermal energy contributions also have a substantial role in favoring H^{ad} on the surface by 0.20 eV, generally shifting reaction intermediates that include H atoms slightly higher than were found with just solvation. We summarize this calculated data in Figure 1.13.

- **O_2 Dissociation:** In the O_2^{ad} dissociation mechanism, dissociation of O_2^{ad} was -1.71 eV downhill in solvent, but it is slightly lower when accounting free energies as well (-1.89 eV). The barrier for this process is calculated similar to the barrier in solvation (0.68 eV). OH^{ad} formation was energetically neutral in solvent with a barrier of 1.14 eV; however, free energy contributions make this value 0.20 eV uphill overall with a similar barrier (1.19 eV). A similar trend is seen with the final formation of H_2O^{ad}. The process is overall $+0.24$ eV in solvent with a 1.10 eV barrier. When accounting for free energies, the same reaction has an overall ΔG_{298K}^{solv} of $+0.55$ eV with a barrier of 1.27 eV.

- **OOH Formation:** In the OOH^{ad} formation mechanism, the energy required to form OOH^{ad} via the Langmuir–Hinshelwood-type reaction of O_2^{ad} and H^{ad} was

0.22 eV in solvent, but including thermal corrections this increases to 0.52 eV. The barrier for this process in solvent alone was 0.94 eV, but with free energy contributions it is slightly higher (1.09 eV). Finally, O–OH dissociation is essentially the same in both solvent (0.62 eV) and after additionally considering thermal corrections (0.59 eV).

- **HOOH Formation:** In the HOOH^{ad} formation mechanism, the energy to further hydrogenize OOH^{ad} via a Langmuir–Hinshelwood-type reaction required 0.27 eV in solvent and 0.68 eV with thermal corrections. Comparable to the formation of OOH^{ad}, the energy barrier to form HOOH^{ad} from OOH^{ad} and H^{ad} is slightly higher when including thermal corrections (1.09 eV compared to 0.94 eV with solvation only). Finally, the barrier for HOOH^{ad} dissociation is slightly lower than in our previous simulations where we included only the water solvent but neglected thermal corrections: 0.31 eV compared to 0.43 eV before.

It is clear that Langmuir–Hinshelwood mechanisms are affected by the motional freedom of H^{ad} on the surface. This stability rising from the presence of H^{ad} impacts relative thermodynamics by making other species containing H atoms relatively less stable by ≈ 0.2 eV. Reaction barriers for this mechanism are not greatly impacted by free energy effects, however.

Eley–Rideal-type reaction profiles with thermal corrections display the same trend shown as solvation-only simulations, which are shown in Figure 1.14. We note that our reliance on the standard state of protons (pH $= 0$) strongly impacts these reaction profiles. After establishing the quantum mechanical energies for these processes, however, one can implement these barriers into a kinetic master equation that
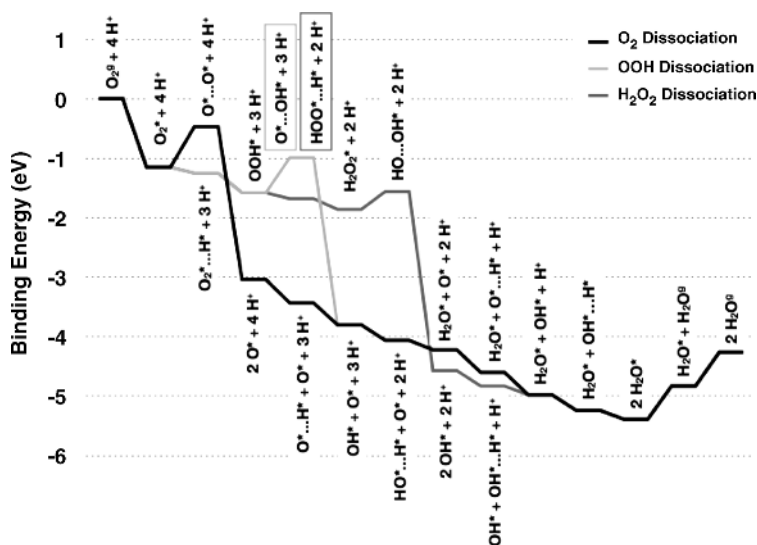
Figure 1.14 Eley–Rideal reactions in water solvent under ambient conditions (including thermodynamic contributions for $T = 298$ K).

depends on the concentration of protons. This type of analysis would be yet another step in moving up the hierarchy of multiscale modeling (see Figure 1.1).

1.3.4
Including an Electrode Potential

Realistic electrochemical systems (such as fuel cells) operate under the influence of an external electrostatic potential difference between the working and the counter electrode. In order to account for the presence of an electrode potential U, different attempts exist to model and understand the structure and properties of systems under electrochemical conditions. An overview can be found in the following reviews [65–68], articles [69–78], and references therein. For the different works mainly experimental input, semiempirical approaches, or quite simplified models are used. The presence of the electrode potential is either neglected or introduced by charging the electrode surface or applying an external electric field. While most of the theoretical studies disregard the presence of an electrode potential, some try to consider its influence on catalytic reactions. For instance, the group of Nørskov [74, 79] studied the hydrogen evolution reaction (HER) and oxygen reduction reaction on different electrodes whose Fermi energies were shifted by the value of the electrode potential. Focusing more on the atomistic structure of the interface, the group of Neurock [76] performed *ab initio* molecular dynamics simulations on charged electrodes surrounded by water. For compensation, a countercharge was located at a certain distance from the electrode surface, trying to mimic the potential profile within the interfacial region.

In order to account for the electrode potential, in the following this effect is approximated by shifting energy levels by a constant value $+e \cdot U$ for every process where a hydrogen (or proton) is dissociated from or attached to a surface species. This influences not only the energies of particular intermediates but also their corresponding transition states, that is, the dissociation or association barriers. Based on this approach, which should be capable to reproduce the overall behavior, Figure 1.15 shows the most favorable (lowest ΔG_{298K} barriers) Langmuir–Hinshelwood and Eley–Rideal processes.

The energy plot makes apparent that both classes of reactions (LH and ER) should be possible at electrode potentials near 1.23 eV, the reduction potential of the ORR established by the Nernst equation. While individual Eley–Rideal reaction barriers appear to be lower than Langmuir–Hinshelwood barriers, the energies for the O^{ad} and OH^{ad} species, which are influential for both classes of reactions, are almost identical and can therefore be expected to be competitive depending on the environmental conditions within the electrochemical system.

In summary, it appears that ORR reaction processes can be reduced to elementary forms of Langmuir–Hinshelwood and Eley–Rideal mechanisms, and treated with high-quality quantum mechanical approaches to obtain relevant thermodynamic stabilities of all species. Further studying the extent that these processes are coupled kinetically is the next logical step to provide insight into the complex ORR mechanism.
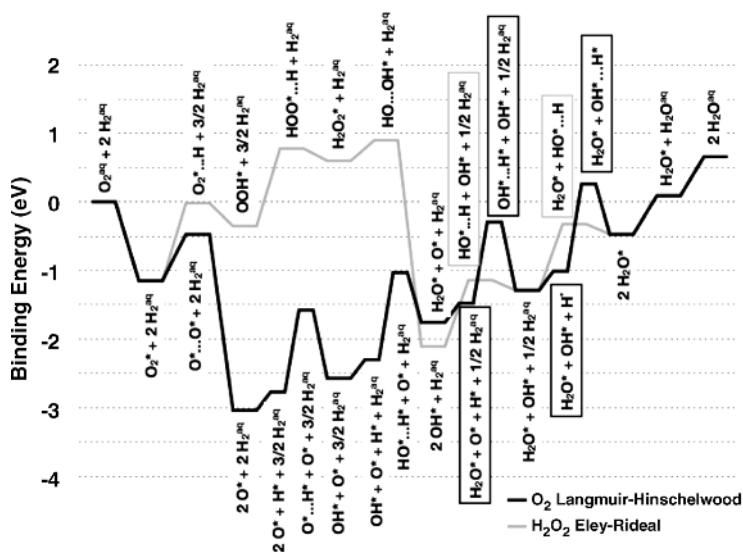
Figure 1.15 Selected (most favorable) reactions under ambient conditions (including solvent and thermal corrections) for an electrode potential of 1.23 V (versus RHE).

1.4
Conclusions

The enormous variety of possible surface reactions reveals many interesting intricacies regarding the ORR mechanisms. Using density functional theory to investigate different mechanisms of the ORR, in this chapter we showed the possibilities of modern *ab initio* modeling and tried to make the readers aware that conclusions might change after including environmental effects and thus should be drawn with special care. Among the three main ORR mechanisms (i.e., O_2^{ad} dissociation, OOH^{ad} formation, and $HOOH^{ad}$ formation), we found that $HOOH^{ad}$ formation is the preferred process in gas phase. When including water solvation as an environmental effect, the reaction paths were modified, leading to drastic changes in the energetics and a nearly identical preference for the O_2^{ad} dissociation and the OOH^{ad} formation mechanisms, but with a blocking of the hydrogen peroxide pathway. Interestingly, inclusion of solvent permits different classes or reaction mechanisms centered around electron transfers and protonations at different electrode potentials. Eley–Rideal variants of the previously investigated mechanisms are all substantially lower in energy at an electrode potential of 0 V. However, inclusion of thermal energy contributions due to ambient conditions, as well an approximate influence of the electrode potential, resulted in a picture showing that both Langmuir–Hinshelwood and Eley–Rideal mechanisms could be at play. Evaluation of the kinetics of all paths should further elucidate the complicated nature of the ORR mechanism.

Acknowledgments

References

1 Born, M. and Oppenheimer, J.R. (1927) *Ann. Phys.*, **84**, 457.

2 Jensen, F. (1999) *Introduction to Computational Chemistry*, John Wiley & Sons, Inc., New York.

3 Groß, A. (2003) *Theoretical Surface Science*, Springer, Berlin.

4 Hartree, D.R. (1927) *Proc. Cambridge Phil. Soc.*, **84**, 457.

5 Fock, V.A. (1930) *Z. Phys.*, **61**, 126.

6 Slater, J.C. (1929) *Phys. Rev.*, **34**, 1293.

7 Dawydow, A.S. (1978) *Quantenmechanik*, Deutscher Verlag der Wissenschaften, Berlin.

8 Dirac, P.A.M. (1930) *Proc. Cambridge Phil. Soc.*, **26**, 376.

9 Bloch, F. (1929) *Z. Phys.*, **57**, 545.

10 Slater, J.C. (1951) *Phys. Rev.*, **81**, 385.

11 Slater, J.C. (1972) *Advances in Quantum Chemistry*, vol. 6, Academic Press, New York.

12 Gaspar, R. (1954) *Acta Phys. Akad. Sci. Hungaria*, **3**, 263.

13 Schwarz, K. (1972) *Phys. Rev. B*, **5**, 2466.

14 Szabo, A. and Ostlund, N. (1989) *Modern Quantum Chemistry*, Dover, New York.

15 Bartlett, R.J. (1989) *J. Chem. Phys.*, **93**, 1697.

16 Møller, C. and Plesset, M.S. (1934) *Phys. Rev.*, **46**, 618.

17 Hohnberg, P. and Kohn, W. (1964) *Phys. Rev.*, **136**, 846.

18 Kohn, W. and Sham, L. (1965) *Phys. Rev.*, **140**, 1133.

19 Thomas, L.H. (1927) *Proc. Cambridge Phil. Soc.*, **23**, 542.

20 Fermi, E. (1927) *Rend. Accad. Lincei*, **6**, 602.

21 Tao, J., Perdew, J.P., Staroverov, V.N., and Scuseria, G.E. (2003) *Phys. Rev. Lett.*, **91**, 146401.

22 Perdew, J.P., Ruzsinszky, A., Tao, J., Staroverov, V.N., Scuseria, G.E., and Csonka, G.I. (2005) *J. Chem. Phys.*, **123**, 062201.

23 Perdew, J.P., Burke, K., and Ernzerhof, M. (1996) *Phys. Rev. Lett.*, **77**, 3865.

24 Slater, J.C. (1974) *Quantum Theory of Molecules and Solids, Vol. 4. The Self-Consistent Field for Molecules and Solids*, McGraw-Hill, New York.

25 Becke, A.D. (1988) *Phys. Rev. A*, **38**, 3098.

26 Vosko, S.H., Wilk, L., and Nusair, M. (1980) *Can. J. Phys.*, **58**, 1200.

27 Lee, C., Yang, W., and Parr, R.G. (1988) *Phys. Rev. B*, **37**, 785.

28 Press, W.H., Teukolsky, S.A., Vetterling, W.T., and Flannery, B.P. (1996) *Numerical Recipes in Fortran 77: The Art of Scientific Computing*, 2nd edn, Cambridge University Press.

29 Gao, J. (1996) *Acc. Chem. Res.*, **29**, 298.

30 Gao, J. (1996) *Rev. Comput. Chem.*, **7**, 119.

31 Car, R. and Parrinello, M. (1985) *Phys. Rev. Lett.*, **55**, 2471.

32 Field, M.J., Bash, P.A., and Karplus, M. (1990) *J. Comput. Chem.*, **11**, 700.

33 Gao, J. and Xia, X. (1992) *Science*, **258**, 631.

34 Dupuis, M., Schenter, G.K., Garrett, B.G., and Arcia, E.E. (2003) *J. Mol. Struct. Theochem.*, **632**, 173.

35 Moriarty, N.W. and Karlstrom, G. (1996) *J. Phys. Chem.*, **100**, 17791.

36 Moriarty, N.W. and Karlstrom, G. (1997) *J. Chem. Phys.*, **106**, 6470.

37 Tomasi, J. and Persico, M. (1994) *Chem. Rev.*, **94**, 2027.

38 Cramer, C.J. and Truhlar, D.G. (1999) *Chem. Rev.*, **99**, 2161.

39 Cossi, M., Mennucci, B., and Cammi, R. (1996) *J. Comput. Chem.*, **17**, 57.

40 Sanner, M.F., Olson, A.J., and Spehner, J.C. (1996) *Biopolymers*, **38**, 305.

41 Eisenberg, D. and McLachlan, A.D. (1986) *Nature*, **319**, 199.

42 Still, W.C., Tempczyk, A., Hawley, R.C., and Hendrickson, T. (1990) *J. Am. Chem. Soc.*, **112**, 6127.

43 Qiu, D., Shenklin, P.S., Hollinger, F.P., and Still, W.C. (1997) *J. Phys. Chem. A*, **101**, 3005.

44 Payne, M.C., Teter, M.P., Allan, D.C., Arias, T.A., and Joannopoulos, J.D. (1992) *Rev. Mod. Phys.*, **64** (4), 1045.

45 Monkhorst, H.J. and Pack, J.D. (1976) *Phys. Rev. B*, **13**, 5188.

46 Jacob, T., Muller, R.P., and Goddard, W.A., III (2003) *J. Phys. Chem. B*, **107**, 9465.

47 Jacob, T., Anton, J., Fritzche, S., Sepp, W.-D., and Fricke, B. (2002) *Phys. Lett. A*, **300**, 71.

48 Jacob, T., Geschke, D., Fritzsche, S., Sepp, W.-D., Fricke, B., Anton, J., and Varga, S. (2001) *Surf. Sci.*, **486**, 194.

49 Jaguar 4.2/5.0, Schrödinger Inc., Portland (2000/2002).

50 Jacob, T. (2006) *Fuel Cells*, **6**, 159.

51 Jacob, T. and Goddard, W.A., III (2006) *Chem. Phys. Chem.*, **7**, 992.

52 Stipe, B.C., Rezaei, M.A., Ho, W., Gao, S., Mersson, M., and Lundquist, B.I. (1997) *Phys. Rev. Lett.*, **78**, 4410.

53 Ho, W. (1998) *Science*, **279**, 1907.

54 Ho, W. (1998) *Acc. Chem. Res.*, **31**, 567.

55 Venkatachalam, S. and Jacob, T. (2009) *Density Functional Theory Applied to Electrocatalysis in Handbook of Fuel Cells: Advances in Electrocatalysis, Materials, Diagnostics and Durability*, vol. 5 & 6 (eds W. Vielstich, H.A. Gasteiger, and H. Yokokawa), John Wiley & Sons Ltd., Chichester, UK, pp. 133–151.

56 Keith, J.A. and Jacob, T. (2009). *Modeling Electrocatalysis from First Principles in Modern Aspects of Electrochemistry, Number 46: Advances in Electrocatalysis* (eds P. Balbuena and V. Subramanian), Springer Heidelberg, Germany.

57 Parker, D.H., Bartram, M.E., and Koel, B.E. (1989) *Surf. Sci.*, **217**, 489.

58 Thiel, P.A. and Madey, T.E. (1987) *Surf. Sci. Rep.*, **7**, 211.

59 Neyerlin, K.C., Gu, W., Jorne, J., and Gasteiger, H.A. (2006) *J. Electrochem. Soc.*, **153**, A1955.

60 Olsen, R.A., Kroes, G.J., and Baerends, E.J. (1999) *J. Chem. Phys.*, **111**, 11155.

61 Jacob, T. and Goddard, W.A., III (2004) *J. Am. Chem. Soc.*, **126**, 9360.

62 Meng, S., Xu, L.F., Wang, E.G., and Gao, S. (2002) *Phys. Rev. Lett.*, **89**, 176104.

63 Ogasawara, O., Brena, B., Nordlund, D., Nyberg, M., Pelmenschikov, A., Petterson, L.G.M., and Nilsson, A. (2002) *Phys. Rev. Lett.*, **89**, 276102.

64 Ruscic, B., Wagner, A.F., Harding, L.B., Asher, R.L., Feller, D., Dixon, D.A., Peterson, K.A., Song, Y., Qian, X.M., Ng, C.Y., Liu, J.B., Chen, W.W., and Schwenke, D.W. (2002). *J. Phys. Chem. A*, **106**, 2727.

65 Schmickler, W. (1996) *Chem. Rev.*, **96**, 3177.

66 Schmickler, W. (1999) *Annu. Rep. Prog. Chem., Sect. C*, **95**, 117.

67 Koper, M.T.M., van Santen, R.A., and Neurock, M. (2003) *Catalysis and Electrocatalysis at Nanoparticle Surfaces* (eds E. Savinova, C. Vayenas, and A. Wieckowski), Marcel Dekker, New York.

68 Koper, M.T.M. (2004) *Ab Initio Quantum-Chemical Calculations in Electrochemistry in Modern Aspects of Electrochemistry No. 36* (eds C. Vayenas, B. Conway, R. White, and M. Gamboa-Adelco), Springer, New York.

69 Nazmutdinov, R.R. and Shapnik, M.S. (1996) *Electrochim. Acta*, **41**, 2253.

70 Halley, J.W., Schelling, P., and Duan, Y. (2000) *Electrochim. Acta*, **46**, 239.

71 Vassilev, P., Hartnig, C., Koper, M.T.M., Frechard, F., and van Santen, R.A. (2001) *J. Chem. Phys.*, **115**, 9815.

72 Haftel, M.I. and Rosen, M. (2003) *Surf. Sci.*, **523**, 118.

73 Feng, Y.J., Bohnen, K.P., and Chan, C.T. (2005) *Phys. Rev. B*, **72**, 125401.

74 Kitchin, J.R., Nørskov, J.K., Barteau, M.A., and Chen, J.G. (2004) *J. Chem. Phys.*, **120**, 10240.

75 Gunnarsson, M., Abbas, Z., Ahlberg, E., and Nordholm, S. (2004) *J. Coll. Interf. Sci.*, **274**, 563.

76 Taylor, C.D., Wasileski, S.A., Filhol, J.S., and Neurock, M. (2006) *Phys. Rev. B*, **73**, 165402.

77 Jacob, T. (2007) *Electrochim. Acta*, **52**, 2229.

78 Jacob, T. (2007) *J. Electroanal. Chem.*, **607**, 158.

79 Rossmeisl, J., Nørskov, J.K., Taylor, C.D., Janik, M.J., and Neurock, M. (2006) *J. Phys. Chem. B*, **110**, 21833.